Metasomatism and cyclic skarn growth along lithological contacts: Physical and geochemical evidence from a distal Pb-Zn skarn

Journal Article

Author(s):
Hantsche, Aaron L.; Kouzmanov, Kalin; Milenkov, Georgi; Vezzoni, Simone; Vassileva, Rossitsa; Dini, Andrea; Sheldrake, Thomas; Laurent, Oscar; Guillong, Marcel ⓘD

Contents lists available at ScienceDirect
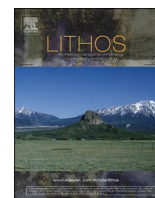
LITHOS

Research Article

Metasomatism and cyclic skarn growth along lithological contacts: Physical and geochemical evidence from a distal Pb—Zn skarn

Aaron L. Hantsche [a,*], Kalin Kouzmanov [a], Georgi Milenkov [a,b], Simone Vezzoni [c], Rossitsa Vassileva [b], Andrea Dini [c], Thomas Sheldrake [a], Oscar Laurent [d], Marcel Guillong [d]

[a] Department of Earth Sciences, University of Geneva, 1205 Geneva, Switzerland
[b] Geological Institute, Bulgarian Academy of Sciences, 1113 Sofia, Bulgaria
[c] Istituto di Geoscienze e Georisorse, CNR, 56124 Pisa, Italy
[d] Institute of Geochemistry and Petrology, ETH Zürich, 8092 Zürich, Switzerland

ARTICLE INFO

ABSTRACT

Distal skarns form by the metasomatic reactions of a host rock induced by far-traveled hydrothermal fluids. Physical and structural characteristics and geochemical patterns of distal Pb—Zn skarn bodies were studied at the Petrovitsa deposit in southern Bulgaria. Skarn bodies formed from the interaction of hydrothermal fluids with reactive host lithologies (marble and gneiss). These fluids were transported along sub-vertical feeder structures and lithological contacts. Epidote skarn developed in gneiss protolith, and pyroxene (johannsenite) skarn developed in marble. Detailed geological mapping, complimented by measurements of the internal structure of the skarn body using pyroxene growth versors, quantifies the propagation direction of the skarn body: 1) away from the major local fluid conduit (feeder structure), and 2) away from lithological contacts between alumi-nosilicate rock and marble. Such growth suggests that fluid flow was generally orthogonal to the skarn front propagation direction in the pyroxene skarn.

Textural, mineralogical and geochemical data from skarn samples reveal multiple growth generations of major skarn calc-silicates epidote and pyroxene. The epidote skarn is characterized by limited spatial distribution and fine-grained epidote/clinozoisite growth associated with massive replacement and sulfide mineralization. The pyroxene skarn consists of acicular clinopyroxene crystals which form spheroidal aggregates with discrete growth banding. These bands are the physical representation of the cyclic fluid pulses which resulted in rhythmic skarn growth marked by geochemical banding. In situ geochemical analyses in the epidote skarn reveal early Al-rich epidote overprinted by Fe-rich epidote associated with higher Mn and Sr contents and irregular compositional banding. Clinopyroxene (Jo_{60-95}) shows general increase in Na, Al, Mn, and REE + Y with distance from the feeder structure and lithologic contacts. These elements correlate with the distance traveled by the hydrothermal fluid from the feeder to the site of skarnification, which we define using a proxy based on the Al content of pyroxene crystals. This reflects an increasing degree of fluid "contamination" by interaction with the aluminosilicate host rocks and functions as a proxy for fluid transport distance. The spatial distribution of trace-elements in pyroxene on an outcrop scale is indicative of discrete pulses of hydrothermal fluid resulting in precipitation of skarn calc-silicates along the increasingly tortuous fluid pathway between the feeder structure and the skarn front, resulting in both the macro- and micro-scale chemical and textural variability of the skarn body.

1. Introduction

Skarns form from the fluid-induced replacement of reactive host lithologies by calc-silicate minerals as a function of host rock composition, fluid chemistry, and overall system temperature (Einaudi et al., 1981; Zharikov, 1970). Metasomatic fluids preferentially destroy and replace reactive minerals (e.g., carbonates) via dissolution-precipitation reactions which allow for additional fluid flow and calc-silicate growth (Korzhinskii, 1968; Yin et al., 2017). This process generates zonation patterns (physical, chemical, and mineralogical) which are used to

categorize skarns based on proximity to fluid source (proximal vs. distal), timing of replacement stages (prograde vs. retrograde), composition (calcic vs. magnesian), and metal endowment (Einaudi and Burt, 1982). Skarns formed from magmatic-hydrothermal fluids can host a wide range of economic metals, which constitute globally significant resource of Fe, Cu, Sn, W, Pb, Zn, Ag, and Au (Meinert et al., 2005). Better understanding of the physical growth mechanisms and geochemical exchange reactions during prograde skarn is needed to improve exploration and exploitation efficiency.

Structural mapping can be used to quantify fluid propagation direction(s) in order to understand relative growth timing of the skarn body. Characterization of major fluid conduits, such as faults, dikes, and lithological contacts, helps to delineate physical distribution of potential ore bodies even at great distances (~10s km) and low water/rock ratios (Megaw et al., 1988; Meinert, 1987). At the outcrop scale, structural mapping sheds light on skarn front propagation, growth processes, and relative timing of events based on internal structures, such as crystal lineations in banded skarns (Vezzoni et al., 2016). Skarn microstructures also provide information on the local P-T-X conditions, yielding evidence for mineral growth mechanisms during skarn formation (e.g., Ciobanu and Cook, 2004; Williams-Jones et al., 2010). These internal structures preserve information on the nature of the lithological contact between skarn and host rock — a feature directly relatable to the reactivity of the host rock (Dipple and Gerdes, 1998). Interpreting paleo-fluid flow and cyclic skarn growth using field and petrographic observations remains the most efficient and cost-effective method of predicting skarn and ore body distribution.

Chemical zoning exists in all skarn systems (e.g., Burt, 1974; Korzhinskii, 1968). Banded skarn silicates result from changes of the physical and chemical parameters of the system, such as temperature, pressure, pH, and/or redox during calc-silicate growth (Chang and Meinert, 2008). Rhythmic chemical bands can form due to compositional layering in the host rock (e.g., organic matter heterogeneous distribution), distinct pulses of metasomatic fluid, or boundary-layer competition for chemical components (Ismail et al., 2014; Vidale, 1969). Thermally and compositionally derived zonation patterns serve as a valuable exploration vector towards more proximal portions of the mineralized system in the porphyry-epithermal environment (Meinert, 1997), and the geochemical signatures of alteration minerals (e.g., chlorite and epidote) in these systems have drawn recent interest (Cooke et al., 2020; Pacey et al., 2020). Similar patterns exist in skarns, but the complex petrogenesis and overprinting mineral assemblages require detailed investigation to determine the metasomatic history of each unique system.

Skarns do not imperatively require a carbonate host to form. In aluminosilicate lithologies, metasomatic reactions can produce epidote-rich skarns with little change in volume and specific gravity identical to that of the host rock (Lentz, 2005). This can occur via bimetasomatic exchange with adjacent lithologies (Zarayskiy et al., 1987) or by the dissolution of original mineralogy, which is replaced by aluminous calc-silicate skarns (Shimazaki, 1982). Because of the influence of host rock geochemistry, skarn formation along a lithological contact can result in drastically different skarn assemblages forming from a single metasomatic event. While metasomatism of aluminosilicate-rich rocks is less voluminous, skarn formation still plays a critical role in the chemical evolution of the whole system.

To better understand skarn growth and zonation patterns, the pyroxene skarns at the Petrovitsa deposit in the Madan Pb—Zn ore field in southern Bulgaria were studied to characterize the prograde evolution of a distal skarn system, which serves as the dominant host for Pb—Zn sulfide mineralization. Detailed structural mapping, petrographic analyses, quantitative mineralogy, and geochemical analyses were combined to discern the relationships between skarn bodies in carbonate and aluminosilicate host rocks with respect to a local feeder structure. In such a controlled setting, this approach was used to trace the progressive evolution of a skarn body at the outcrop, hand sample, and microscopic

scale and to decipher the physical and chemical processes that govern the prograde formation of mineralized distal skarn systems.

2. Geological setting

The Madan ore field in southern Bulgaria (Fig. 1) hosts polymetallic Pb—Zn (± Ag, Cu) deposits which have produced more than 100 Mt. of ore since 1940, with average grades of 2.54 wt% Pb and 2.1 wt% Zn, with Cu and Ag by-products (Milev and Ivanov, 1996). The ore field is hosted in the uplifted basement sequence of the central part of the Rhodope Massif (Fig. 1B), in the exposed Gondwana-derived metamorphic basement (Schmid et al., 2020). The Central Rhodopian dome is exposed by a series of low-angle detachment faults that juxtapose tectonic units of different metamorphic grades (Kounov et al., 2020). The lower plate of the detachment system is comprised of an orthogneiss composed of late Paleozoic granitoids metamorphosed at upper amphibolite to granulite facies (Peytcheva et al., 2000). The upper unit, the Madan Unit, is composed of biotite gneiss, locally migmatized, with layered metagabbros (amphibolites) and marble lenses (Sarov et al., 2007). The Asenitsa Unit, to the north, is composed of lower-amphibolite facies biotite gneiss and thick marble units (Kounov et al., 2020). Crustal thickening and peak metamorphism in the Central Rhodopian tectonic units occurred in the Cretaceous to Paleogene in an active Tethyan arc setting which had ceased compression by the Eocene (Burg, 2011).

Peraluminous Eocene granitoids (Smilian Granite: Fig. 1B), mark the beginning of post-collisional extension in the region (Kaiser-Rohrmeier et al., 2013). Pegmatite intrusions (35.70 ± 0.23 Ma; U—Pb dating on monazite; Ovtcharova et al., 2004) mark the end of Eocene extension and uplift, but subaerial magmatism continued, expressed geologically as rhyolite dikes and ignimbrite deposits beginning at 31.70 ± 0.18 Ma (U—Pb dating on zircon; Ovtcharova et al., 2003) and continuing into the mid-Oligocene in the Smolyan Basin to the north. Skarn formation and sulfide mineralization in the Madan ore field post-date extension along the Madan detachment, and has been constrained between 31.41 ± 0.39 Ma (U—Pb dating on zircon; Hantsche et al., 2017) and 29.95 ± 0.23 Ma (Ar—Ar dating on hydrothermal muscovite; Kaiser-Rohrmeier et al., 2004).

A series of NW-trending, post-detachment, transtensional fault systems controls the mineralization in the Madan ore field (Fig. 1B). The Madan ore field hosts Pb—Zn sulfide mineralization which is observed dominantly as vein- or skarn-hosted deposits. In aluminosilicate-rich hosts, mineralized faults generally produce vein-style mineralization (Bonev and Piperov, 1977). Conversely, faults running through marble lenses within the Madan Unit contain mineralization expressed as skarn- and carbonate-hosted deposits (Vassileva et al., 2009). Radiogenic isotope tracing on sulfides has been used to propose a genetic model for the hydrothermal system, suggesting that crustal melting associated with extension generated hydrothermal fluids and provided a heat source for meteoric fluid circulation, retaining Pb and S isotopic signatures of sulfides that match the host rock (Marchev et al., 2005; Marchev and Moritz, 2006). No systematic relationship has been discovered between mineralization and related intrusive units at depth. Post-mineralization *E*-W extensional faults cross cut all lithologies and mineralization in the district.

3. Geology of the PETROVITSA deposit

Located 5 km south of the town of Madan, the Petrovitsa deposit is situated on a northwest-trending regional structure and is one of six remaining mining operations within the Madan ore field (Fig. 1C). The deposit is hosted in the Madan Unit biotite gneiss complex, with interbedded marble and amphibolite units forming discontinuous lenses up to 10 m-thick (Fig. 1C). The foliation direction of the metamorphic sequence is highly variable, but can be generally constrained as dipping to the south-west at 30°-40°. Both *syn*-metamorphic (~ 50 Ma according
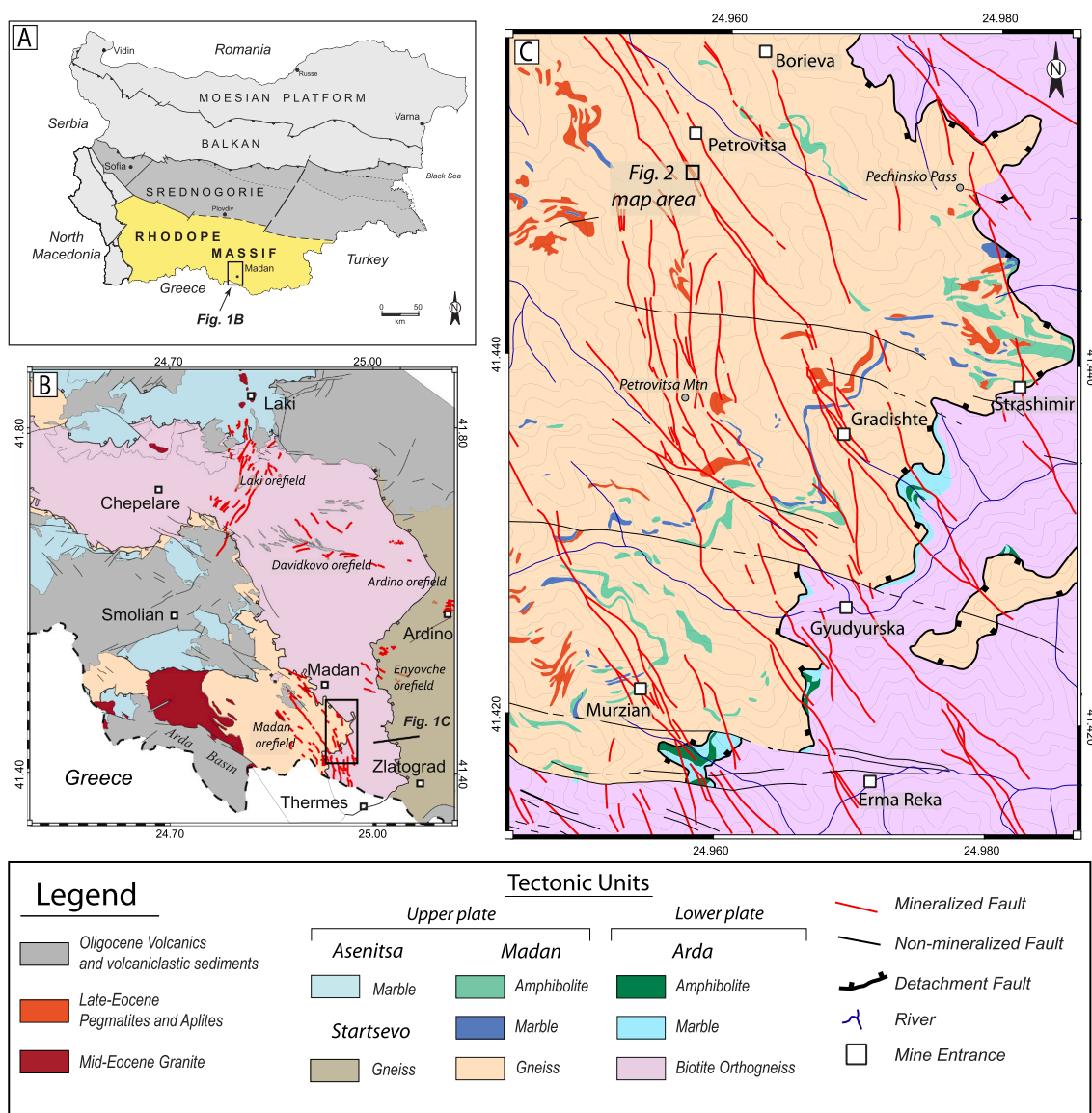
Fig. 1. (A) Map of tectonic units of Bulgaria (modified from Dabovski et al., 1991). (B) Regional geologic map of the Central Rhodopes (after Kounov et al., 2020). (C) District-scale geologic map with deposit locations (from Ivanov et al., 1987).

to U—Pb ages on titanite: Milenkov et al., 2020) and post-metamorphic (35.89 ± 0.20 Ma U-Pb dating on monazite; Ovtcharova et al., 2003) pegmatite intrusions are observed. The major fault system at Petrovitsa is a syn-mineralization NW-SE trans-tensional primary structure, which is traceable for up to 2.5 km, with sulfide mineralization extending from surface (~1250 m above sea level, m.a.s.l.) to the lowest working level (600 m.a.s.l.) which is crosscut by post-mineralization E-W extensional faults (Kostova et al., 2004). Mineralized veins have Pb/Zn ratio > 2 and contain early quartz, epidote, and chlorite, with later precipitation of sulfides, primarily galena, sphalerite, pyrite, chalcopyrite, arsenopyrite, and pyrrhotite, along with quartz, carbonates, and muscovite (Milenkov et al., 2019; Vassileva and Bonev, 2003). The skarn-hosted ore bodies form where these veins or splays crosscut the conformable marble lenses and where fluid exploited lithological contacts, generally limited by the vertical thickness of the marble units (Fig. 2; Vassileva et al., 2009).

3.1. Skarns of the Petrovitsa Deposit

The most impressive skarn bodies in the Madan ore field are composed of Mn-rich calcic clinopyroxene which extend 10's of meters away from the mineralized veins into the marble lenses (Fig. 2B; Vassileva, 2004; Hantsche et al., 2019). The skarn bodies form along contacts between the marble and the feeder structure, as well as along lithologic contacts between gneiss (or pegmatite) and marble (Fig. 2B and C). The pyroxene skarns are composed of radial spheroidal aggregates of elongated pyroxene crystals diverging from central nucleation points (Fig. 3). In large skarn bodies, these radial aggregates have grown together, amalgamating into a massive pyroxene skarn with irregular growth bands, partially terminated spheroidal aggregates, and scallop or cauliflower textures terminating sharply at the classic "knife-edge" skarn front.

Retrograde replacement of the prograde skarn occurs most heavily near lithological contacts and mineralized feeder structures. Texturally, the overprinting by retrograde minerals occurs along grain boundaries and bands of fine-grained clinopyroxene which are first altered by pseudomorphic/interstitial replacement, followed by texturally destructive, massive overprinting by retrograde skarn minerals (Vassileva et al., 2009). The retrograde mineral assemblage consists of a mixture of fine-grained calcite + quartz + rhodonite + rhodochrosite + bustamite + chlorite + Mn-amphibole ± K-feldspar and is associated
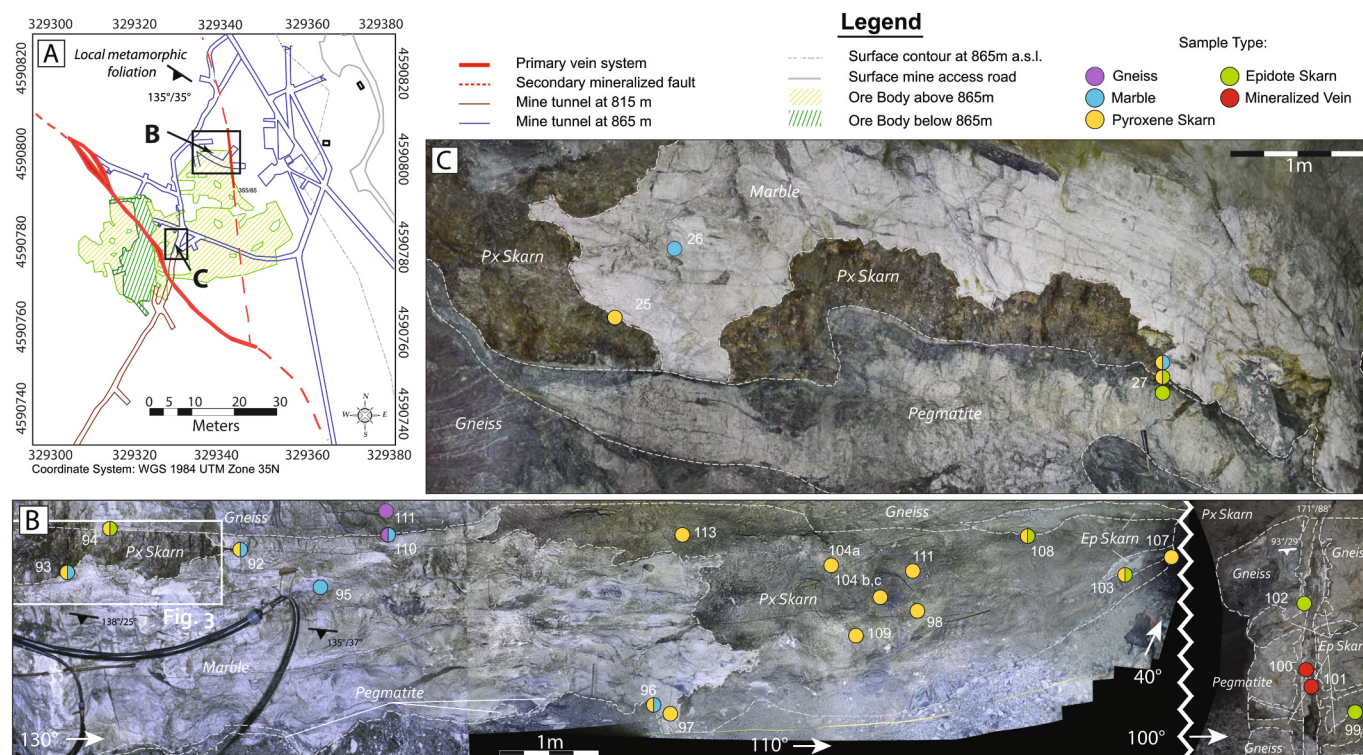
Fig. 2. (A) Plan view map of part of the Petrovitsa mine horizon 865 m. (B) Photogrammetry view and sample locations of a skarn-feeder system at the Petrovista 865 m North outcrop. (C) Photogrammetry view and sample locations of skarn along lithological boundaries between gneiss, pegmatite and marble at the Petrovitsa 865 m South outcrop. Abbreviations: Ep – epidote; Cpx - clinopyroxene.

with sulfide mineralization which is dominated by sphalerite + galena + pyrite + chalcopyrite (Milenkov et al., 2019; Vassileva and Bonev, 2003).

In the aluminosilicate-rich host rocks such as gneiss and pegmatite, metasomatic replacement of original minerals produces epidote skarns, which are described at the Petrovitsa deposit for the first time. Due to the impermeable nature of the host rock, epidote skarns rarely extend more than 1 m away from the lithological contacts and fault structures which served as major conduits for the mineralizing fluids. Fluid transport within the host was controlled by the secondary permeability generated during skarn formation (Ortoleva et al., 1987a), which favored the metasomatism of feldspar-rich pegmatites and melanocratic bands of the gneiss. Replacement occurs in two styles – selective replacement along foliation planes or massive replacement of the host. Sulfide mineralization occurs in the open space generated during skarn formation and consists of sphalerite, galena, chalcopyrite, and pyrite (Kolkovski and Manev, 1988).

3.2. Mineralizing Fluids

The best constraints on the physicochemical parameters of the mineralizing fluid at Petrovitsa indicate that the earliest quartz generation synchronous with sulfide precipitation (Q1; 280°-320 °C) entrapped a neutral, low-salinity fluid (average salinity of 4.5 wt% NaCl equiv.) with only trace concentrations of metals (median composition: 128 ppm Mn, 102 ppm Zn, and 3 ppm Pb; Kostova et al., 2004). Sulfide precipitation is interpreted to have been triggered by an influx of meteoric water late in the lifespan of the hydrothermal system (Kotzeva et al., 2011). Hydrodynamic modeling of the system is coherent with the thermal maturation of a magmatic heat source and the associated circulation of hydrothermal fluids(Driesner and Geiger, 2007). Novel work using the 3D morphology and crystal growth patterns of quartz indicate a shift in fluid directions, supporting the influx of meteoric water influencing Pb and Zn sulfide precipitation (Milenkov et al., 2019).

4. Sampling and analytical methods

A combination of geologic mapping and structural measurements of a distal skarn body has been used to constrain the position of the samples used for optical microscopy, QEMSCAN, laboratory XRF whole rock and portable XRF (pXRF), EPMA and LA-ICP-MS techniques for major, minor and trace element mineral geochemistry. Detailed analytical methods are reported in Appendix 1.

4.1. Geologic Mapping, Versor Measurements, and Sampling

Geological mapping of the outcrop was done using photogrammetry and high-resolution outcrop mapping methods at 1:20 scale. Oriented samples were taken for textural, petrographic, and chemical analysis (Fig. 4A and B; Appendix 2).

Mineral growth versors were first identified as an indicator of skarn propagation direction by Vezzoni et al. (2016) in the banded skarns at Campiglia Marittima (Italy). Elongate skarn minerals were shown to record skarn growth towards open space generated by fluid flow along a single fracture zone. Growth versor mapping was applied to the Petrovitsa 865 m North skarn body to interpret the propagation sense and timing of the skarn front in 3D. Lineation measurements (i.e., plunge and plunge direction) of 411 individual pyroxene crystals were made in the skarn body which extends up to 15 m from the mineralized feeder vein (Fig. 4A and B). The full dataset is reported in Appendix 3. All measurements were made on the well-exposed skarn body on the west side of the mineralized fault. Pyroxene crystals were selected based on available measurement surfaces, and measurements were grouped into domains based on their position on the outcrop (near the upper contact, at center, near the lower contact: Fig. 4C). Most measurements were made on coarse-grained pyroxene (more than 2 cm in length) and spaced apart by 3–5 cm. For each domain, every individual crystal that could be measured meeting the above criteria was recorded, with accepted biases of grain size and geometric constraints of the outcrop. Because the
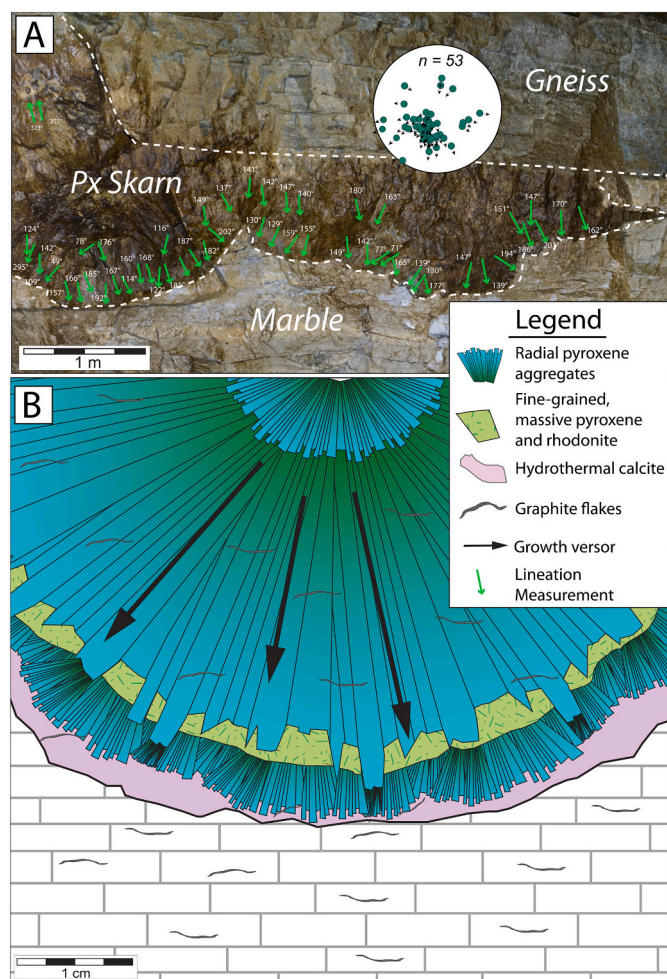
Fig. 3. (A) Pyroxene growth versor measurements from a distal skarn body, with lineation measurements plotted on a stereonet projection (location indicated in Fig. 2B), where arrows indicate the sense of the unidirectional growth versor. (B) Cartoon diagram of pyroxene spheroidal aggregates growth with textural and compositional banding ending at a sharp skarn front.

massive texture of the skarn body, no preference was given to crystal orientation relative to the skarn front, as was done in the previous study (Vezzoni et al., 2016). Orientation data were plotted on stereographic projections and a rose diagram to assess outcrop scale growth direction (Fig. 4B and C).

4.2. Optical petrography and QEMSCAN analysis

A standard optical transmitted- and reflected-light petrographic study was carried out on the selected samples; detailed descriptions, images, and mineral maps can be found in Appendix 2. Detailed information on QEMSCAN mineral mapping, data acquisition and processing can be found in Appendix 1.2.

4.3. Bulk Rock analyses

Whole-rock measurements were performed by wavelength dispersive X-ray fluorescence (XRF) spectrometer PANalytical Axios^{mAX} fitted with a 4,0 KW Rh X-ray tubeon glass pellets at the University of Lausanne, Switzerland for major element compositions. Trace element compositions were determined on the same glass pellets by using an Inductively Coupled Plasma – Mass Spectrometer (ICP-MS) coupled to an excimer laser system at ETH Zürich. In situ measurements were also made using Thermo Fischer Niton XL3t portable XRF with an 8 mm spot

size. Whole-rock methodology is reported in Appendices 1.3 and 1.4, and data tables can be found in Appendix 4.

4.4. In-situ Mineral analyses

Major element compositions of pyroxene and epidote were measured using a JEOL 8200 Superprobe at the University of Geneva, Switzerland. Measurement conditions used an accelerating voltage of 15 kV with a current of 20 nA, and a beam diameter of 1 μm. Detailed methods and data treatment are reported in Appendix 1.5. Trace-element compositions of pyroxene and epidote were determined using a RESOlution excimer ArF (193 nm) laser ablation system with a spot size of 19 μm coupled to an Element XR sector-field ICP-MS. Detailed methodology can be found in Appendix 1.6. All in-situ geochemical results are reported in Appendices 6 and 7.

5. Results

5.1. Physical Skarn Growth

Mineralized skarn systems preserving clear structural relationships linking skarn bodies to a feeder structure (865-North) and growth along a conformable pegmatite-marble contact (865-South) were discovered (Figs. 2 and 4). The mineralized feeder vein (N 350°) is a splay of the primary structure of the Petrovitsa deposit and is directly associated with metasomatic replacement of both carbonate (pyroxene skarn) and aluminosilicate (epidote skarn) rocks (Figs. 2B and 4). Both skarns exhibit varying degrees of retrograde overprint and sulfide mineralization.

Spatial measurements were made to locate each sample: the distance from the feeder vein (DF), calculated by taking the shortest distance to the feeder structure, and the distance from the lithological contact (DC), the shortest measured distance to the aluminosilicate-rich rock. The relative timing of each sample was constrained by combining distance measurements with the pyroxene versor measurements (Fig. 4B and C).

Pyroxene growth versors indicate a westward crystal growth direction, orthogonal to the feeder structure (Fig. 4B). Groups of versor measurements show clusters of data indicating two general growth directions: 1) away from the feeder structure, and 2) away from the lithological contacts. Therefore, the thickness of the skarn body is directly linked to the timing of growth, and the oldest parts of the skarn body formed closest to these structures.

5.2. Petrography and Quantitative mineralogy

Detailed sample descriptions and petrographic data can be found in Appendix 2.

(i) Marble: Unaltered marble lenses are characterized by coarse-grained calcite with often abundant graphite flakes defining the metamorphic foliation. Rare phlogopite and pyrite are present (<1 vol%), and rare calcite (± chlorite) veins <1 mm cut across some parts of the marble.

(ii) Gneiss: Unaltered gneiss is dominated by quartz, plagioclase, K-feldspar, foliation-defining biotite (partially altered to chlorite + titanite near the contact between gneiss and marble). All titanite in these samples is replaced by Ti-oxides prior to skarn formation, referred to hereafter as the mineral mixture leucoxene (Lx).

(iii) Skarns: A generalized comparison between the two skarn types can be found in Table 1.

Epidote skarn: Epidote skarn is dominated by massive epidote replacement of aluminosilicate minerals that decreases in volume with distance from the fluid conduit (Fig. 5A). Epidote crystals are small and euhedral (generally <2 mm), with early epidote found along with K-feldspar replacing plagioclase (often albite) using the host minerals as reaction surfaces (Fig. 5B). This early assemblage of epidote + K-feldspar is overgrown by a later assemblage that includes epidote + quartz ±
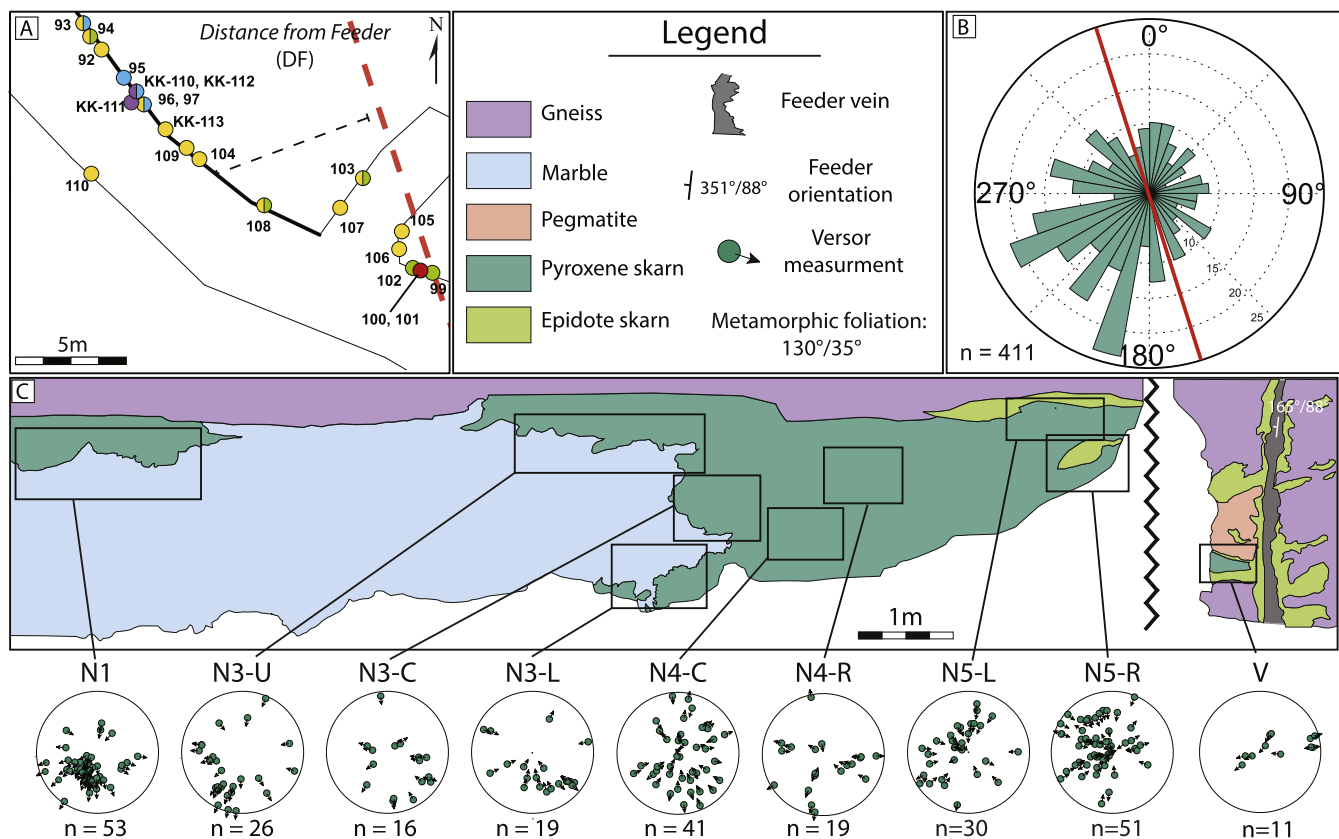
Fig. 4. (A) Plan view map and sample location of skarn-feeder study area. (B) Rose diagram of measured pyroxene versors at Petrovitsa 865 m North, including data from the south wall and the northeast-trending adit. Data available in Appendix 2. (C) Geologic sketch of the north wall of the 865 m North gallery and versor measurements reported on stereonet projections. Arrows indicate the sense of the unidirectional growth versor. (For interpretation of the references to colour in this figure legend, the reader is referred to the web version of this article.)

calcite; these epidote generations will hereafter be referred to as epidote 1 and 2, respectfully (Figs. 5B-D). Epidote 2 can be seen as an overgrowth on early epidote 1 (Fig. 5D) and as cavity infill (Fig. 5E). Muscovite (texturally, sericite) replaces K-feldspar, and chlorite replaces epidote (both generations). A retrograde assemblage of epidote + quartz + calcite is also found in the mineralized feeder vein in sample MN-101B, in which early pyroxene has been destroyed (Milenkov et al., 2019).

Pyroxene skarn: Pyroxene skarns are composed of spheroids formed by radial aggregates of calcic clinopyroxene replacing the carbonate host (Fig. 5F). Clinopyroxene nucleates and grows towards open space along fluid conduits (Fig. 5G) often generating hemispherical aggregates of radially-disposed crystals grown sequentially to create a cauliflower-like crown at the skarn-marble contact or where spheroidal aggregates collide (Fig. 5H). The prograde skarn front terminates sharply against the marble, and is characterized by a boundary layer of quartz, rhodonite, and recrystallized carbonate (Fig. 5F). Pyroxene can grow up to 10 cm-long, and terminates sharply at the contact with the marble, either as fibrous needles or prismatic crystals with flat terminations hosted in hydrothermal calcite and quartz (Bovay, 2016). Inert graphite flakes from the marble are trapped during skarn growth, roughly retaining the original metamorphic foliation. Subsequent generations of pyroxene create new bands, which are frequently distinguished by crystal size or composition (Fig. 5F and H).

Retrograde overprint begins with the pseudomorphic replacement of euhedral pyroxene crystals following the sequence of rhodonite ± amphibole ± bustamite ± chlorite (e.g., Capitani et al., 2003). Calcite, quartz, and in some cases, adularia, crystallized in pore spaces generated during the breakdown of pyroxene to amphibole and chlorite. QEMS-CAN mineral mapping reveals that the pseudomorphic replacement and interstitial infill are followed by massive, fine-grained replacement that destructively overprints the cyclic banding (Fig. 5J).

Sulfide Mineralization: Sulfide mineralization of the skarn bodies overlaps with retrograde skarn formation. Mineralization occurs in both epidote and pyroxene skarns, and is found along fluid pathways, commonly the skarn front, near the feeder, or in interstices generated by the destruction of preexisting skarn minerals (Figs. 5E, J). Sulfide mineralization occurs in three stages: 1) quartz + pyrite, 2) quartz + sphalerite + galena ± chalcopyrite, and 3) pyrite + calcite. While these sulfides dominate the assemblage, a complete detailed list of accessory phases can be found in Kolkovski and Manev (1988). Continued sulfide mineralization results in the textural destruction and massive overprint of the skarn bodies (Fig. 5J).

5.3. Whole Rock Geochemistry

Whole rock geochemical analyses show drastic increase in the Mn, Fe, and Si content of the pyroxene skarn, accompanied by a loss of Ca when compared to the host marble. In the epidote skarn, the contents of Ca, Fe, and Mn increase, while Na is removed with respect to the unaltered gneiss. Portable XRF measurements reveal an influx of Ca to the gneiss, accompanied by an increase in the content of K, Rb, and Ba near the contact. Bulk rock XRF and pXRF analyses and profiles can be found in Appendices 4 and 5.

5.4. Pyroxene Mineral Chemistry

5.4.1. Major element geochemistry

Major element analyses indicate pyroxene compositions in the ternary calcic clinopyroxene solid solution series johannsenite

Table 1
Textural features and mineral composition of epidote and pyroxene skarns at the Petrovitsa Pb—Zn deposit.

		Epidote Skarn		Pyroxene Skarn	
		Textures	Mineralogy	Textures	Mineralogy
Prograde		• Irregular distribution in gneiss and pegmatite (Fig. 5A) • Foliation controlled or massive replacement (Fig. 5B) • Pale pink or pistacchio green color replacing host (Fig. 5A) • Thin fractures perpenduclar to foliation (Fig. A2.23) • Coarse grained (1-2mm) epidote crystals • Epidote replacement of plagioclase feldspar and biotite Fig. A1.18) • Smaller crystals with distance from conduit • `Leucoxene precedes skarn formation (Fig. 5E)	Epidote (1) K-feldspar ±quartz	• Radial aggregates of elongate, acicular pyroxene crystals reaching up to 10 cm • Pyroxene nucleates at fluid conduit, grows in marble (Fig.5G) • Blue/Green pyroxene oxidized to dark green/brown (Fig. 5F) • Sharp "knife edge" contact with marble (Fig. 5I) • Growth bands determined by grain size (Fig. 5H) • Pyroxenes terminate as prismatic crystal faces OR fine accicular fibers •1-2mm thick band of recrystallized calcite at skarn front • Graphite flakes encapsulated by skarn pyroxene (Fig. 5J)	Ca-pyroxene ± rhodonite
Retrograde		• Veins cross cutting other structures (Fig. 5B) • More volumnous epidote replacement (Fig. A1.23) • Epidote 2 crystal overgrowth of Epidote 1 (Fig. 5D) • Accicular needles of Epidote 2 grow into open space with quart (Figs. 5C-D)	Epidote (2) quartz calcite	• Pale brown in color • Loss of internal structures (Fig. A2.24) • Quartz and calcite form interstitially in the degrading pyroxene spheroids (Fig. A2.11) • Rhodonite pseudomorphic replacement of pyroxene at skarn front (Fig. 5I) • Destructive replacement by massive fine-grained carbonates	Quartz calcite amphibole rhodonite chlorite ±adularia ±rhodochro- site ±sphalerite
Mineralization		• Sulfide in cavities from complete destruction of feldspars (Fig. 5C) • Epidote replaced by chlorite (Fig. 5B-C) • K-feldspar replaced by sericite FIg. 5B)	calcite quartz sericite chlorite galena sphalerite pyrite ± chalcopyrite	• Massive replacement of retrograde skarn • Weak, crumbly material composed of clay and calcite • Infil into cavities and interstices within the skarn body	calcite quartz sericite chlorite galena sphalerite pyrite ± chalcopyrite

$[CaMnSi_2O_6]$ – hedenbergite $[CaFeSi_2O_6]$ – diopside $[CaMgSi_2O_6]$ (Fig. 6A). EMPA data from 1358 point analyses show that most pyroxene in this study is Mn-rich, with Mn^{2+} spanning from 0.17 to 0.98 a.p.f.u. (atoms per formula unit), correlating inversely with the Fe^{2+} content (up to 0.38 a.p.f.u.). Clinopyroxene composition varies with both *DF* and *DC*, and with the crystal length (Figs. 6A-B). The average pyroxene composition is Jhn_{77} Hd_{18} Di_5 and higher Mn contents are observed with increasing *DC* and *DF*. Elemental maps produced using QEMSCAN show distinct Fe/Mn ratios in pyroxene growth bands for certain samples (Appendix 2), which is supported by high-resolution quantitative EPMA mapping and backscattered electron (BSE) imaging (Figs. 6C-F). Major element maps of individual crystals show a sharp boundary between core ($Jhn_{79}Hd_{19}Di_2$) and rim ($Jhn_{59}Hd_{26}Di_{15}$) (Figs. 6C-E). Cumulatively, these data highlight the wide range of clinopyroxene compositions generated during each skarn growth event, defined by

compositional, textural, and grain size variations (hereafter referred to as a growth cycle: see discussion in section 6.3).

5.4.2. Trace element geochemistry

Clinopyroxene (708 analyses) has relatively low abundances of trace elements (generally <10 ppm), the most common of which are shown in Fig. 7, where the data are grouped in function of distance measurements, *DF* (Fig. 7A) and *DC* (Fig. 7B). Magnesium and Al are the only minor elements detected in the clinopyroxene, and Na and Zn are the only trace elements with concentrations higher than hundreds of ppm (Fig. 7). Certain trends are observed with increasing distance from the feeder (decrease in Mg, Ti, V, and Co; Fig. 7A), which differ when data are sorted by distance from the lithological contact (Fig. 7B), highlighting the impact of fluid transport distance.

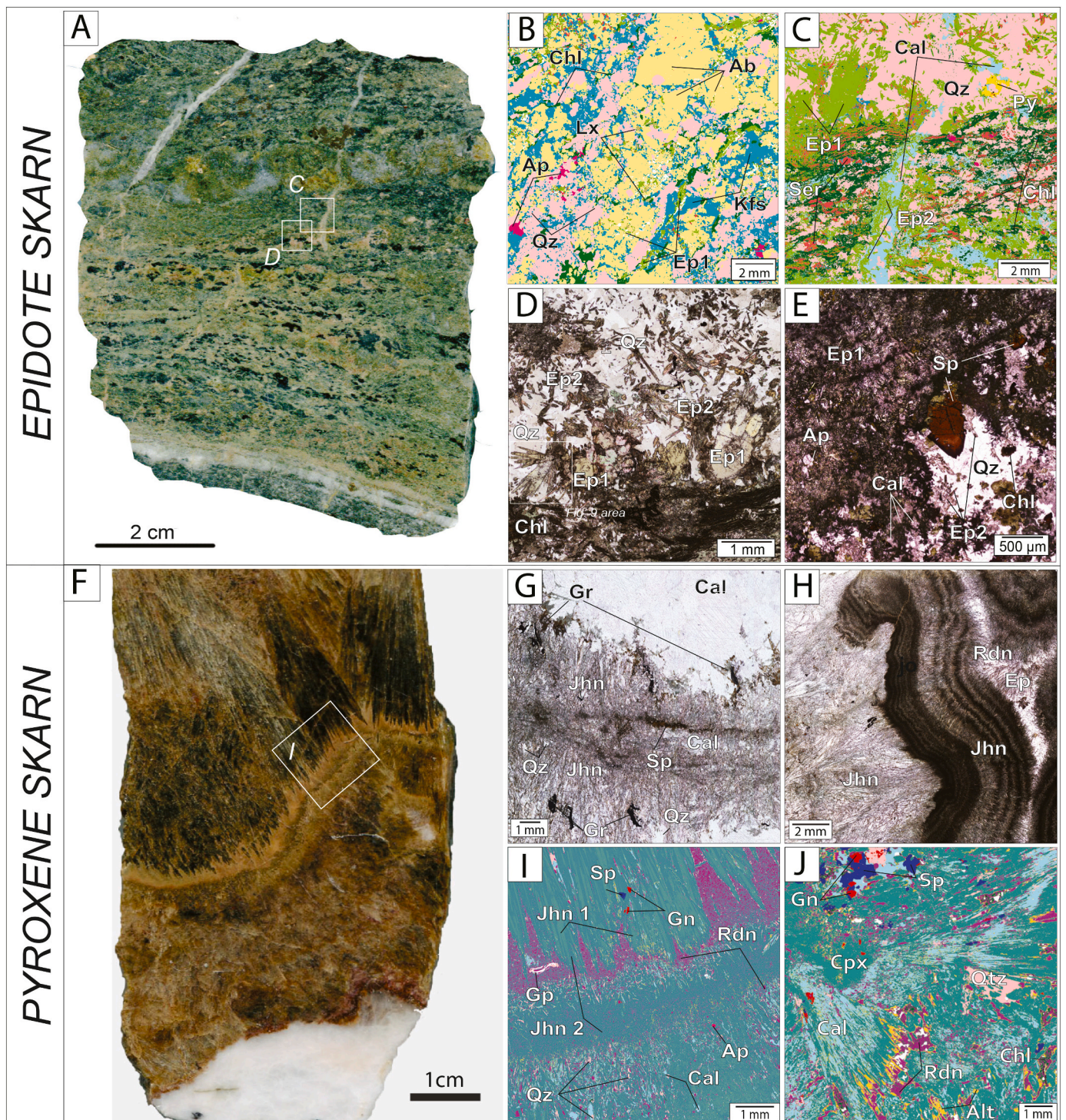The BSE image in Fig. 8A shows that both clinopyroxene generations

Fig. 5. (A) Hand-sample photo of foliation-controlled epidote skarn (MN-102). (B) QEMSCAN mineral map showing early replacement of albite in the protolith by K-feldspar and epidote (MN-103e). (C) QEMSCAN mineralogy highlighting late epidote growth with calcite in a vein (MN-102v). (D) Epidote 1 and subsequent overgrowth by fine-grained euhedral epidote 2 hosted in quartz (MN-102v, PPL photomicrograph). (E) Secondary porosity in epidote skarn infilled with retrograde and sulfide minerals (MN-108a, PPL photomicrograph). (F) Hand-sample photo of banded pyroxene skarn in marble (MN-25). (G) Pyroxene skarn growing bidirectionally into marble from a fluid conduit (MN-96b, PPL photomicrograph). (H) Fine-grained cyclic banding of late pyroxene spheroids terminating against each other resulting in interstitial cavity (MN-94c, PPL photomicrograph). (I) QEMSCAN mineral map highlighting textural and chemical banding within a banded pyroxene skarn (MN-25b). (J) QEMSCAN mineral map of retrograde skarn alteration and sulfide mineralization (MN-98a). Abbreviations after Whitney and Evans (2010): Ab – albite, Alt – johannsenite altered by calcite, Ap – apatite, Cal - calcite, Chl - chlorite, Cpx – clinopyroxene; Ep - epidote, Gn – galena, Gr - graphite, Jhn - johannsenite, Lx – leucoxene, Py - pyrite, Qz - quartz, Rdn - rhodonite, Ser – sericite, Sp – sphalerite.
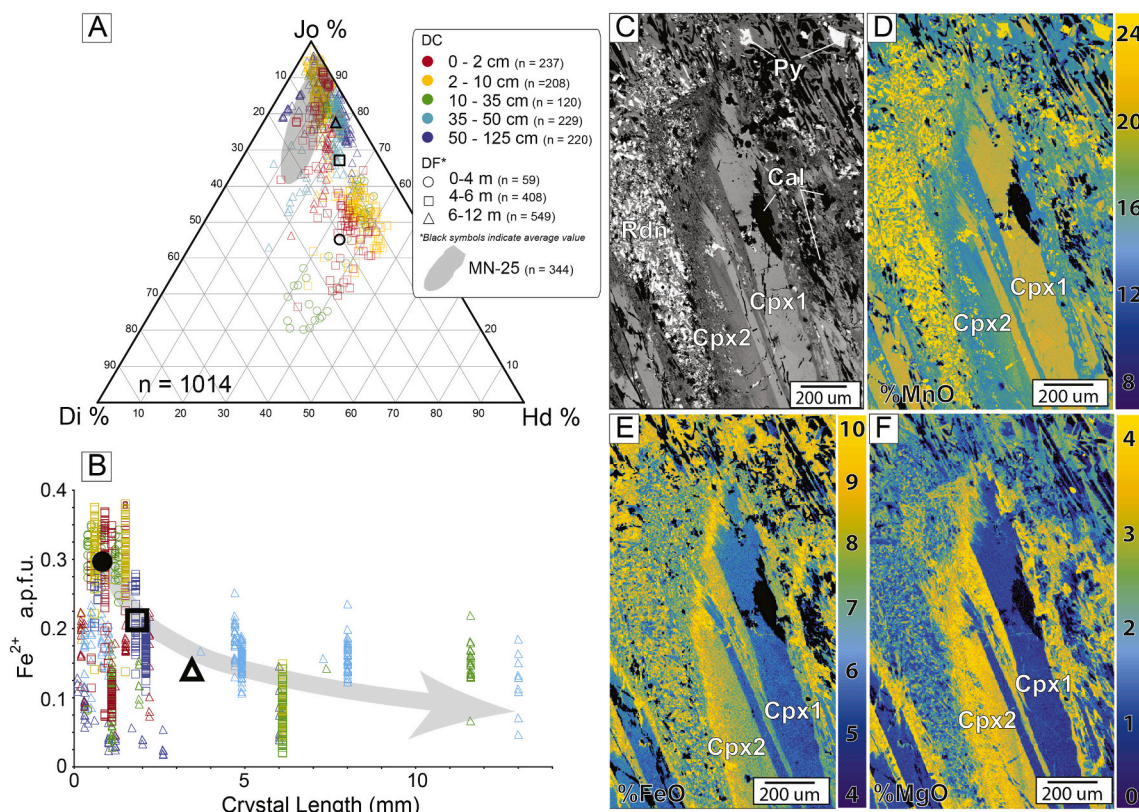
Fig. 6. (A) Pyroxene compositions from Petrovitsa 865 m North outcrop plotted on calcic-clinopyroxene ternary diagram. Data from EPMA. (B) Crystal size vs. Fe (a. p.f.u.) plot for pyroxene. (C) BSE image of pyroxene crystal at growth band interface. (D—F) EPMA elemental map in wt% of MnO (D), FeO (E), and MgO (F). Abbreviations: Cal - calcite, Cpx – clinopyroxene, Py – pyrite, Rdn - rhodonite.
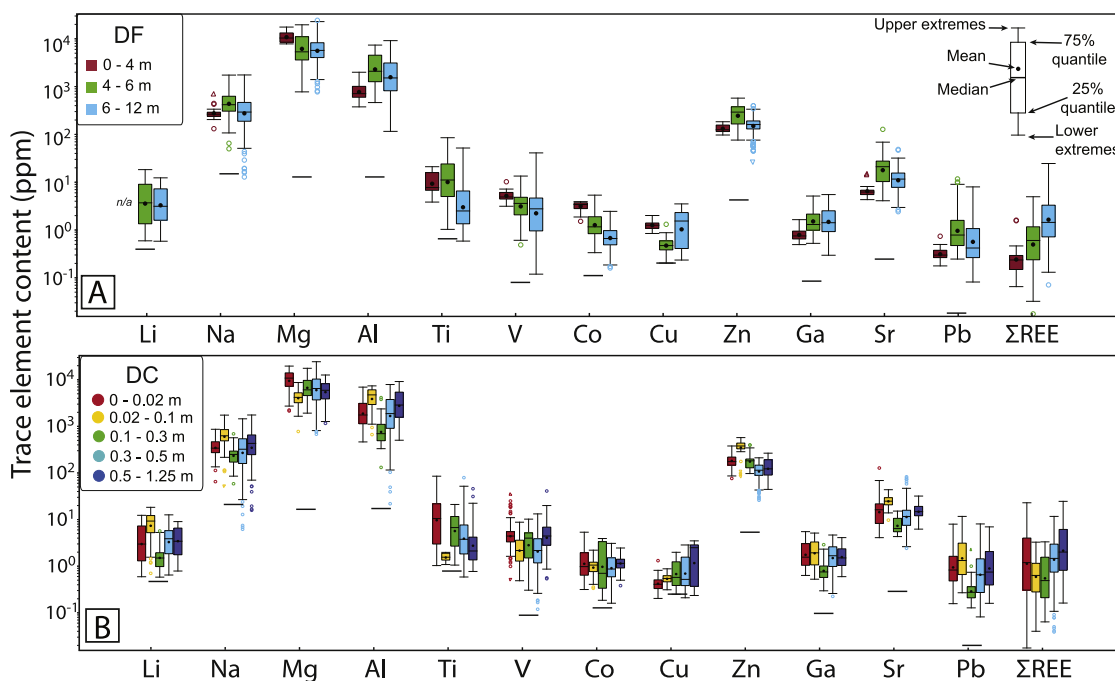

Fig. 7. Box plots of selected trace element contents in pyroxene from LA-ICP-MS data. (A) Sorted by distance from feeder (DF). (B) Sorted by distance from contact (DC). Lower horizontal marks correspond to the average limits of detection (LOD) for each element.
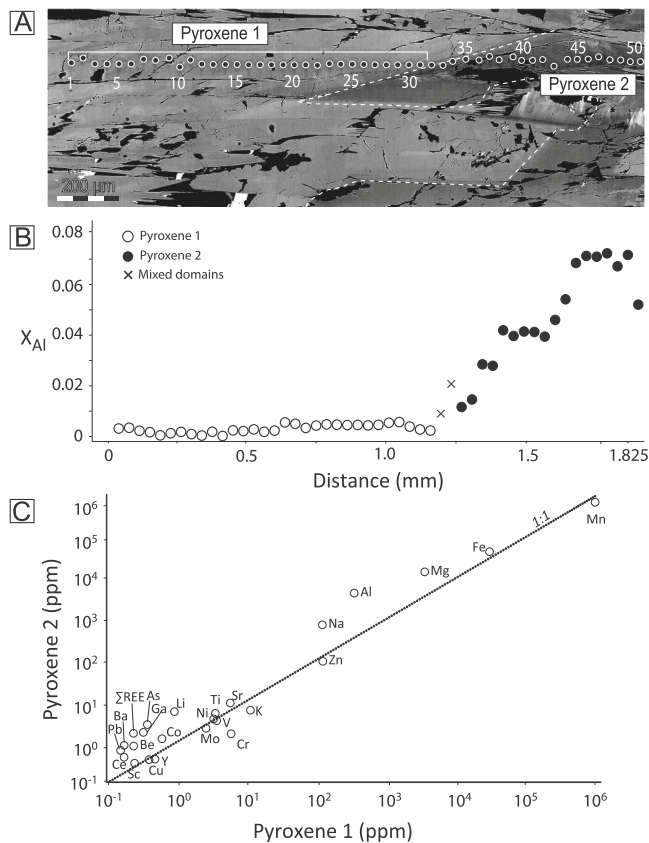
Fig. 8. (A) BSE image and LA-ICP-MS profile outlining pyroxene generations (MN-25b). (B) LA-ICP-MS data showing mole fraction of Al (X_{Al}). (C) Average element content in pyroxene 1 and pyroxene 2 based on LA-ICP-MS analyses (MN-25b).

formed during a single cycle can be differentiated by their Al content (Fig. 8B). Trace elements are preferentially incorporated into clinopyroxene 2 (Fig. 8C). There is no evidence for sector zoning along specific crystal axes. The dataset of chemical results on pyroxene can be found in Appendix 6.

5.5. Epidote Mineral Chemistry

Major element geochemistry. Epidote major element data (777 analyses) fall within the clinozoisite [Ca_2 (Al^{3+})$_3$(SiO_3)$_4$OH] - ferriepidote [Ca_2 (Fe^{3+}_2, Al^{3+})(SiO_3)$_4$OH] solid solution series due to direct exchange of Al^{3+} and Fe^{3+} in the M-site of the crystal structure (Fig. 9A; see Armbruster et al., 2006). Epidote 1 (427 analyses) is more aluminous in all samples, with mean values for Al^{3+} of 2.31 a.p.f.u. and for Fe^{3+} of 0.68 a.p.f.u. In contrast, epidote 2 (350 analyses) has an average composition for Al^{3+} of 2.18 a.p.f.u. and for Fe^{3+} of 0.80 a.p.f.u (Fig. 9A). Clear relationships between different epidote generations can be observed in transmitted light and BSE images, combined with high-resolution EPMA maps. Which illustrate the compositional differences between epidote 1 and epidote 2 overgrowth (Figs. 9D-F).

5.5.1. Trace element geochemistry

Epidote trace element analyses (n=301, Fig. 10) show that epidote 1 is characterized by higher contents of Mg, Ti, and Zn and lower contents of Mn, Sr, and Pb than epidote 2. Rather, the shift in Mn/Mg ratio is a definitive feature of the two epidote crystallization events, correlating with base metal (Pb and Zn) and Sr content (Fig. 10B).

The average of ΣREE (+ Y) is about two times higher than that of pyroxene, but still fails to meet the hundreds of ppm ΣREE (+ Y) present

in the whole rock, which is principally hosted in metamorphic apatite and other accessory phases. The REE patterns, separated by sample and epidote generation (Fig. 10D), are characterized by relatively flat slopes ($La_N/Yb_N = 1.15$) and moderately positive Eu anomalies (Eu/Eu* = 2). The full dataset of epidote geochemical results can be found in Appendix 7.

6. Discussion

The massive Petrovitsa skarns formed due to fluid flow along the primary NW-trending mineralized fault and its subsidiary splays where these conduits intersected reactive carbonate rocks and exploitable lithological contacts. Cyclic pulses of over-pressured fluid resulted in hydraulic fracturing along such contacts, forming skarn on either side. While this was limited by reactivity and permeability in aluminosilicate-rich host rocks, widespread skarn growth in the marble occurred due to the dissolution and subsequent generation open-space. Using the structural and geochemical results obtained in this work, it is possible to explore the mechanisms of skarn formation and fluid propagation at both macro- and micro-scale.

6.1. Skarn Front Propagation in Massive Skarn Bodies

The validating principles of skarn front propagation in banded skarns (Vezzoni et al., 2016) hold true in the massive skarn bodies at the Petrovitsa deposit. Pyroxene versor measurements quantify the crystal growth direction parallel to the longest axis and perpendicular to the ancient skarn front, which creates the convex shape of the pyroxene spheroids (Abrecht, 1985; Rusinov and Zhukov, 2008). Therefore, silicate growth initially occurred along the lithological contacts, as well as along the contact with the feeder (Fig. 4). The two directions of skarn growth were primarily perpendicular to either: 1) the feeder structure, or 2) lithological contacts between marble and aluminosilicate-rich lithologies (gneiss, pegmatite). These two modes of skarn growth were approximately concurrent, implying that skarn thickness corresponds to relative age of formation. Skarn minerals formed near fluid conduits at the boundary of the carbonate rock (low DF/DC) represent early precipitation and relatively short fluid transport distances. Conversely, pyroxene crystals from the center of the marble lens formed later, precipitating from fluid which traveled longer distances prior to metasomatic pyroxene growth.

Pyroxene lineation measurements should not be mistaken to represent fluid flow direction, as they only record the crystallization direction of pyroxene during skarn growth. Similar growth textures occur in natural settings in igneous systems in which acicular pyroxene crystals form rapidly from an undercooled melt. Spinifex textures, defined by the acicular crystallization of olivine or pyroxene in komatiites, occur due to strong thermal gradients and rapid crystal growth towards chemical nutrients along the long axis (Arndt and Fowler, 2004). Experimental studies found that pyroxene nucleation does not occur until these systems were significantly undercooled, triggering oriented crystallization in the [001] direction (Bouquain et al., 2014; Faure et al., 2006). While there are no studies on the nucleation and growth of hydrothermal pyroxene, the radial texture of pyroxene aggregates suggests limited nucleation followed by an explosion of rapid growth of skeletal pyroxene crystals in the direction of chemical nutrients, i.e., the fluid flow boundary along the knife-edge skarn marble contact. Rapid growth textures are also observed at the microscopic scale as [001] growth twins and polysomatic fractures in other manganoan pyroxene skarns (Capitani et al., 2003). A similar formation mechanism for the prograde skarn textures is proposed in this study, in which undercooling and cyclic hydrothermal activity at Petrovitsa resulted in rapid bursts of pyroxene growth that generated the typical banded texture of the prograde pyroxene skarns.

Existing skarn models often invoke fluid flow through preexisting skarn prior to the dissolution and metasomatic growth of new skarn
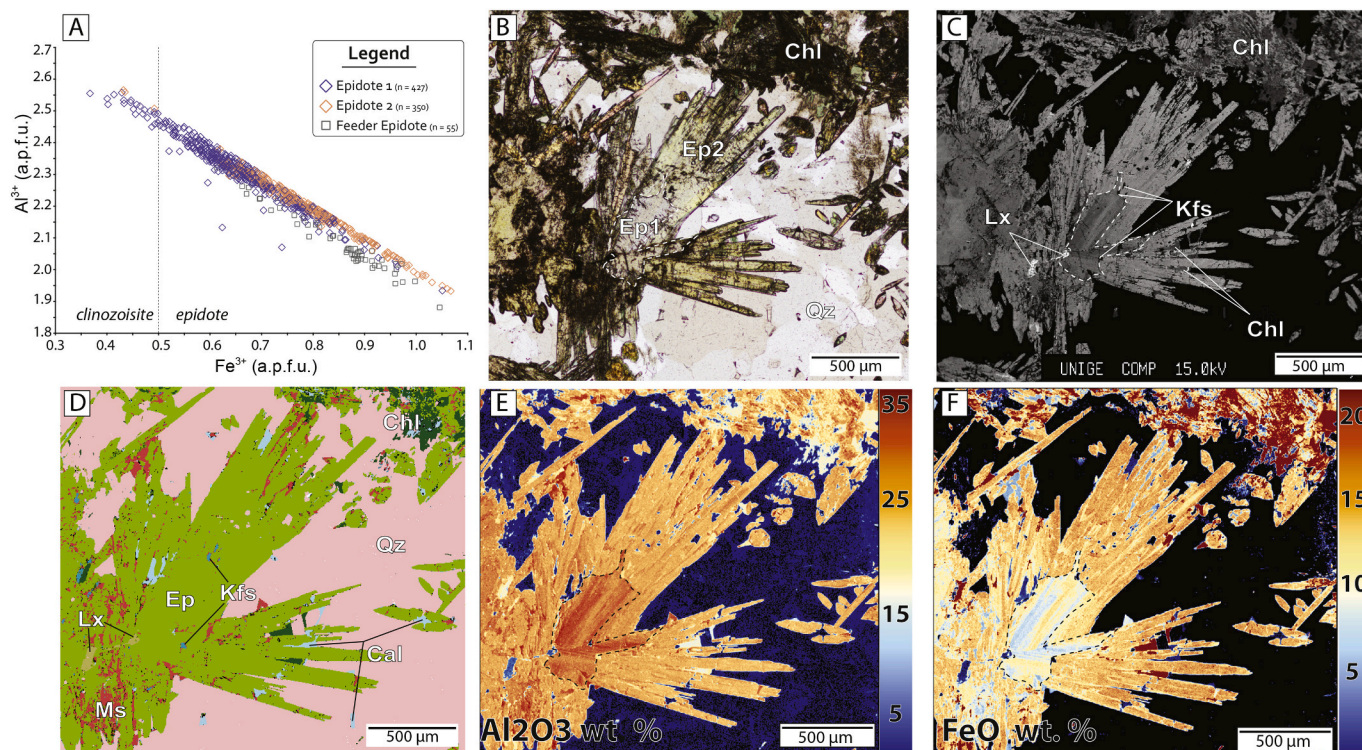
Fig. 9. (A) Fe vs Al (a.p.f.u.) compositional plot of epidote, based on EPMA data. Feeder epidote data from Milenkov et al. (2019). (B) Epidote 1 with euhedral epidote 2 overgrowth in a quartz vein (PPL photomicrograph). (C) BSE image highlighting fine-grained mineral assemblage associated to epidote skarn formation. (D) QEMSCAN mineral map supporting early epidote associate with K-feldspar. Note relict leucoxene enveloped by epidote. (E) EPMA elemental map of Al₂O₃ (wt%). (F) EPMA elemental map of FeO (wt%). Abbreviations: Cal – calcite, Chl - chlorite, Ep - epidote, Kfs - K-feldspar, Lx - leucoxene, Qz – quartz, Ms. – muscovite.

minerals (Meinert, 1992; Meinert et al., 2005). This may occur in more permeable skarn bodies (i.e., garnet skarns), but detailed structural mapping indicates little evidence for fluid propagation through skarn bodies at Petrovitsa. Rather, fluid flow was apparently perpendicular to the crystal growth direction and parallel to the skarn front, meaning that metasomatic fluids propagation and skarn formation into a reactive unit is actually the "side" of the system (Yardley and Lloyd, 1995).

6.2. Fluid pathway and transport parameter

Following the argument above, the continuous and irregular expansion of the skarn front requires that later fluids exploited a longer, more tortuous pathway along lithological boundaries prior to arriving at the pyroxene nucleation site. Longer transport distances exposed these fluids to higher degrees of fluid-rock interaction, which is recorded in pyroxene mineral chemistry by changes in the Fe/Mn ratio and Al content of clinopyroxene at thin section, hand sample, and outcrop scale.

The complete range of Fe/Mn and Al contents from entire outcrop are contained within clinopyroxene from a single sample located about 6 m from the feeder (MN-108; Figs. 11A-B). The clinopyroxene chemistry can be split into two distinct groups based on the linear relationship between Fe/Mn and Al content. The first (low-gradient) group is characterized by larger variability in Fe/Mn content. These pyroxene crystals are adjacent to the aluminosilicate contact and exhibit poorly developed pyroxene spheroids and finer grain size (Figs. 11C-D). The second (high-gradient) group is characterized by larger variability in Al content, and it is comprised of often coarse-grained johannsenite crystals with higher DC values (Fig. 11E). These pyroxenes are likely to have grown from a "non-pristine" hydrothermal fluid which incorporated more Al during interaction with the aluminosilicate host rocks.

For the two groups identified above, the spread of data within a single sample is related to chemical variability at crystal scale. The

gradient of the slope, however, is a function of the fluid pathway during transport from the main conduit to the site of skarn formation. Hydrothermal fluids that were transported along lithological contacts produce clinopyroxene with higher Al content, suggesting that X_{Al} value increases with the fluid transport distance. The "contamination" of Al in the metasomatic fluid is accompanied by the decrease in Fe/Mn ratio at outcrop scale, as Fe is consumed earlier along the fluid flow path (e.g., pyroxene closer to the feeder is more ferric). Consequently, the slope between Fe/Mn and Al content for a single sample can be used as a proxy for degree of fluid-rock interaction. The early pyroxene skarn which occurred near the contact formed from a fluid with a much shorter transport distance than the later skarn (MN-108d; Appendix 2).

All other measurements from the Petrovitsa deposit lie between the two indicated slopes in Fig. 11B, exhibiting positive correlation in the Al – Fe/Mn space, and increasing Al contents with increasing DC and DF values. These relationships suggest that the geochemical signature of a pyroxene can be used as a *transport parameter (TP)*,

$$TP = \frac{X_{Al} \times X_{Mn}}{X_{Fe.}}$$

which reflects fluid-rock interactions that occurred along the marble-gneiss boundary prior to skarn formation. Higher degrees of contamination from the aluminosilicate rock explain the increase of the Al content of pyroxene with DC. Critically, this is built on the assumption that fluid arriving from the feeder at any given time is uniform and that TP records changes occurring in fluid chemistry *after* the fluid transportation along the feeder structure from a deeper source. Hydraulic fracturing and exploitation of the lithological contacts allow fluid-rock interactions which result in generally higher TP values for samples with longer fluid transport distances (Fig. 12A-B). Sodium, Ga, ΣREE (+ Y) correlate positively with the average TP, while Co and Mg, among others, have inverse correlation trends (Fig. 12B; Appendix 8). The overall chemical evolution at the outcrop scale is a product of
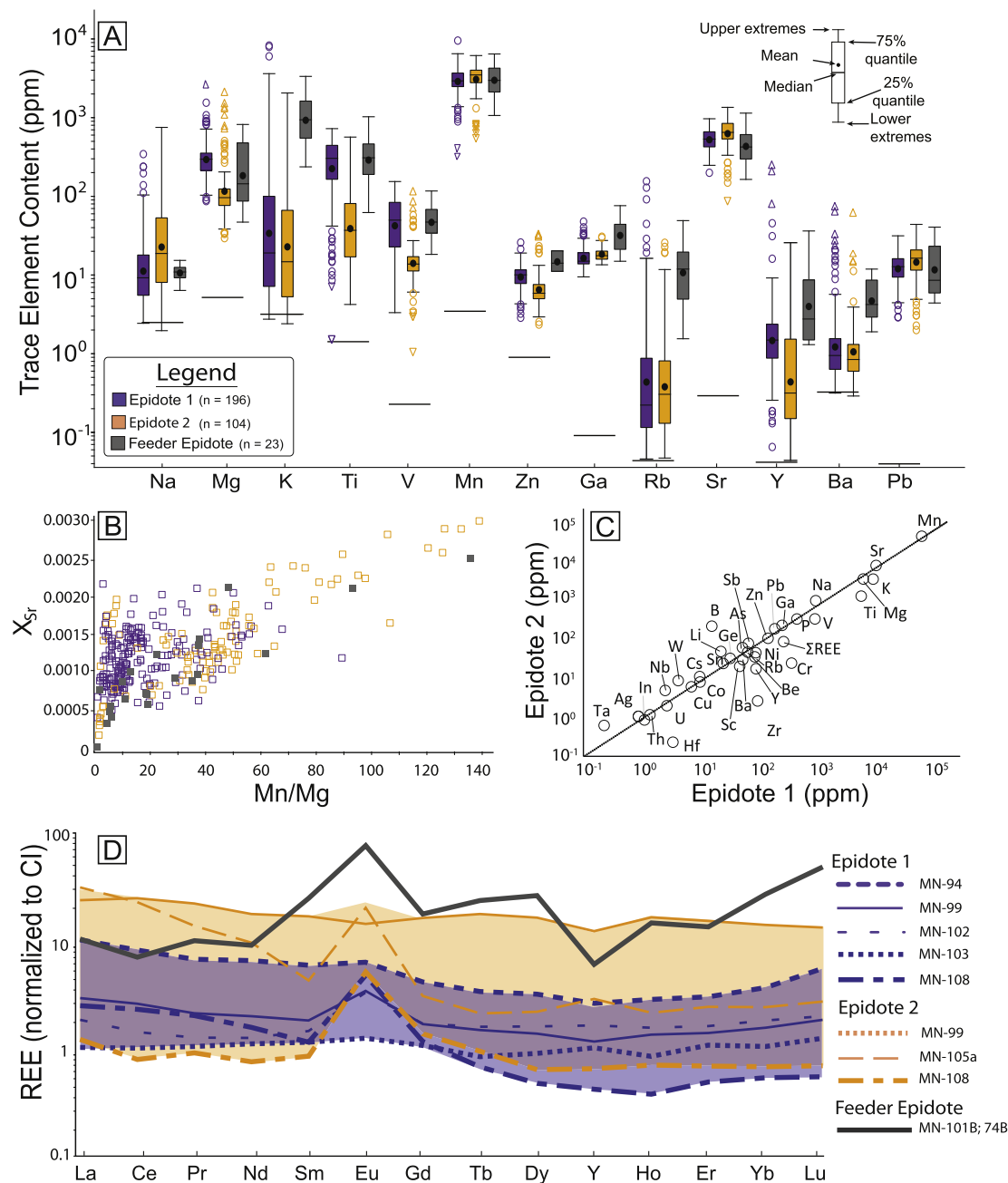
Fig. 10. (A) Box plot of trace element composition of epidote from Petrovitsa 865 m North outcrop sorted by generation. Lower horizontal marks correspond to average limits of detection (LOD) for each element. (B) Molar abundance of Sr vs. Mn/Mg ratio plot. (C) Trace element contents in epidote 1 vs. epidote 2. (D) Average REE pattern for epidote by sample and generation. REE values normalized to chondrite (Sun and McDonough, 1989)

progressive evolution achieved through cyclic banding during successive skarn growth events.

6.3. Cyclic formation and geochemical evolution of pyroxene skarns

The importance of cyclic growth banding of pyroxene skarns cannot be understated. Many skarn systems exhibit banded textures at multiple scales, as compositional growth zones or repeating grain size variations (Guy, 1993; Jiang, 1993; Xu et al., 2016). The absence of compositional zoning in the host marble at Petrovitsa, requires that chemical and physical banding occurred in one of two manners: 1) open system growth via pulses of chemically distinct metasomatic fluid, or 2) closed system growth in which bands form from geochemical competition resulting in a self-organized structure. While both require reactive

infiltration and undergo similar crystallization sequences, self-organizing structures cannot, by definition, be formed by the constant introduction of external fluids (Guy, 1993).

Each growth cycle, composed of multiple pyroxene generations with distinct geochemical compositions, begins with the formation of open space via dissolution of the carbonate minerals of the host marble. This follows a positive-feedback loop in which dissolution results in increased fluid flow, which in turn results in increased dissolution (Ortoleva et al., 1987b). The introduction of new fluid to the system suggests that open system behavior is responsible for textural and chemical features at the growth cycle scale. The mechanisms of precipitation within a growth cycle, behave in a closed system (or "steady-state") manner, governing geochemical variations within the growth band.

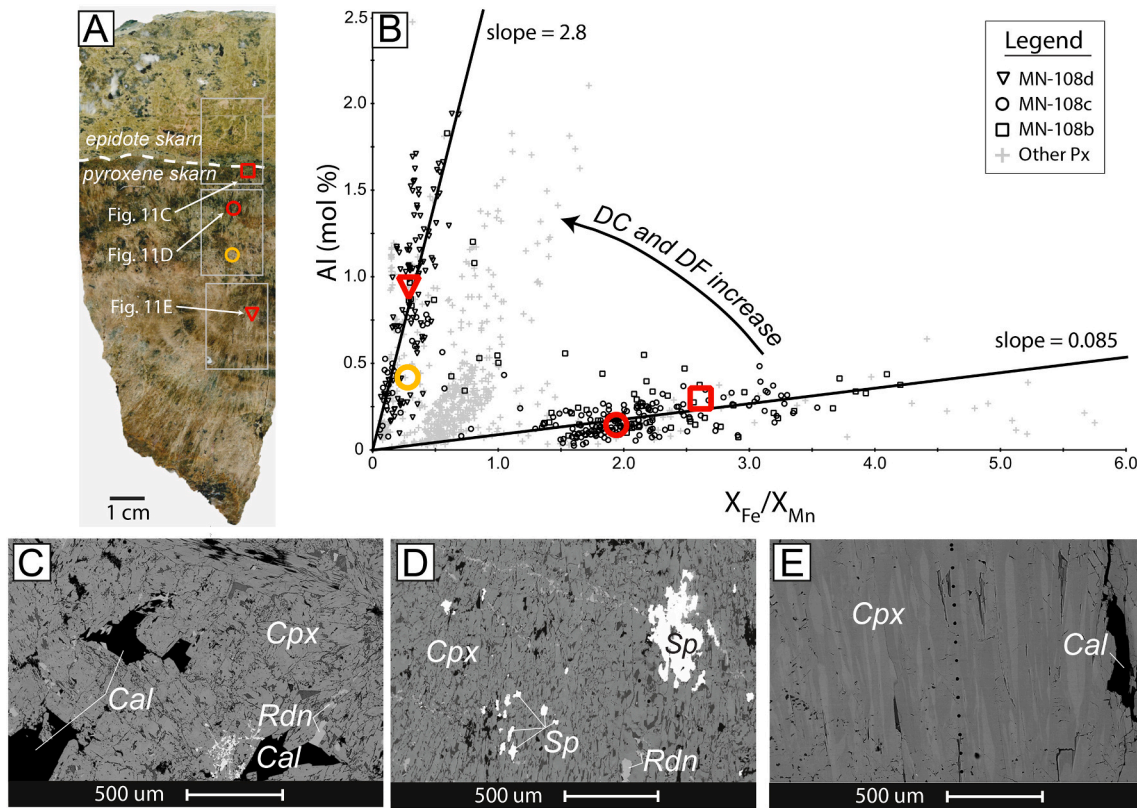The open space associated with initial dissolution reactions is

Fig. 11. (A) Hand-sample along a pyroxene-epidote skarn boundary (sample MN-108). Thin section locations along a transect across the boundary are indicated. (B) Fe/Mn molar ratio vs. Al mole % plot, used to define TP (see main text for explanation). (C) BSE image of pyroxene aggregate close to the contact (MN-108b). (D) BSE image of lower portion of intermediate sample (MN-108c). (E) BSE image of more distal banded pyroxene skarn (MN-108d). Abbreviations: Cal - calcite, Cpx - clinopyroxene, Rdn - rhodonite, Sp - sphalerite.
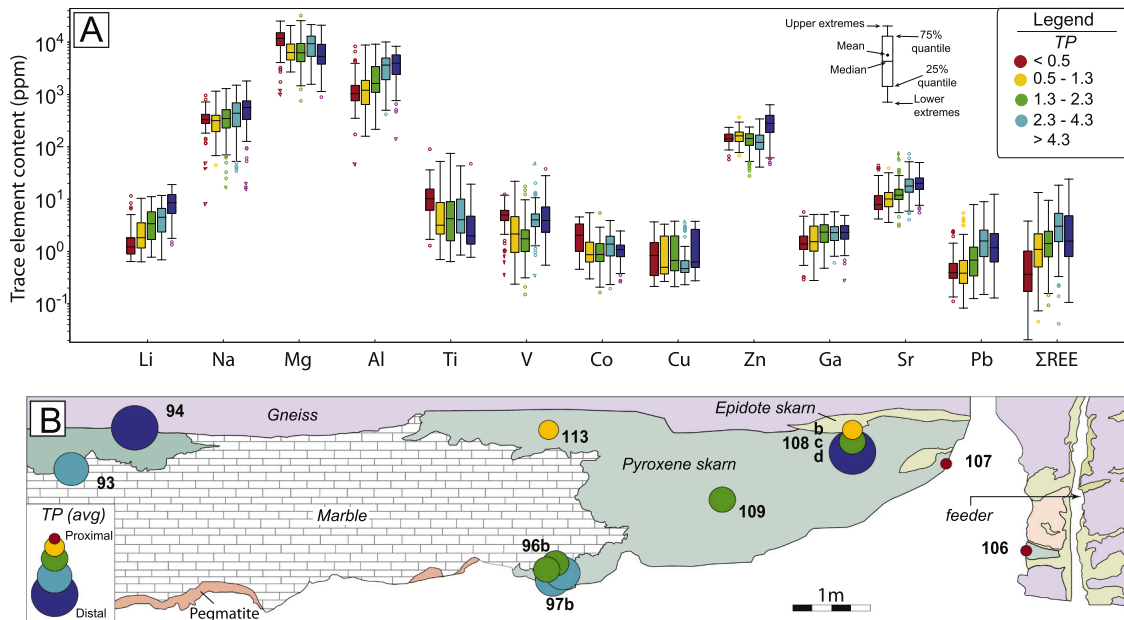

Fig. 12. (A) Trace element content of pyroxene sorted by Transport Parameter (TP). (B) Outcrop geology and sample location highlighting the link between physical distance from the feeder with increasing TP.

coupled with subsequent precipitation reactions following a path of supersaturation → nucleation → depletion (Jiang, 1993; Ortoleva et al., 1987a; Yin et al., 2017). The repetition of pyroxene generations, clinopyroxene 1 (Jhn$_{75-85}$) overgrown by clinopyroxene 2 (Jhn$_{55-65}$), is the

geologic evidence of this mechanism during each cyclic growth event. The skarn front, marked by prismatic crystals or tiny fibers of pyroxene, served as a nucleation surface for the next skarn mineral growth. This mechanism has been attributed to self-organizing structures in skarns

due to boundary layer chemical competition during mineral growth (Korzhinskii, 1968). These dissipative structures begin each growth cycle formed by a supersaturated fluid which rapidly nucleates mineral (s) and depletes the boundary layer in specific chemical components (Guy, 1993). Consecutively, crystallization at the boundary layer adjusts naturally, new phases precipitate incorporating the residual chemical components from oversaturated fluids.

Without the input of new fluid, the activity of Mn (α_{Mn}) in the fluid prevailed over the activity of Fe (α_{Fe}), allowing for high-Mn johannsenite (pyroxene 1 - $Jo_{75–85}$) to grow first and larger. Finer-grained, more ferrous johannsenite (pyroxene 2 - $Jo_{55–65}$) crystallizes at the end of cycles, when the α_{Mn} is diminished. This occurred systematically and repeatedly at local scale, producing alternating, cyclic chemical bands recorded by the Fe/Mn ratio of the pyroxene within a single pyroxene generation as a product of boundary layer depletion (Fig. 13). Sample MN-94c (Fig. 5H; Appendix 2) exhibits a rhythmic banding texture which requires that each fluid pulse was ephemeral in nature, allowing for closed-system processes in a relatively stagnant fluid and the formation of a new skarn front. The closed system processes will continue to control pyroxene crystallization in this manner as long as there are adequate i) chemical components, ii) thermodynamic favorability, and iii) open space.

While the pyroxene chemical composition and banding record shifts in local fluid chemistry (Abrecht, 1980), textural differences shed light on the open system behavior during the subsequent fluid pulses. Changes in pyroxene grain-size represent the end of a growth cycle, leaving a static skarn front and a stagnant fluid until the next infiltration of metasomatic fluid. Growth bands with larger grain sizes result from periods of sustained skarn growth and higher volume of fluid flux. When a new fluid enters the skarn system, rapid nucleation will again be governed by the dominant chemical component of the system, in this case Mn. The overall availability of Fe in the system limits the growth of the more ferrous clinopyroxene 2 ($Jo_{55–65}$) to smaller grain sizes. Modeling of micro-scale chemical heterogeneity in clinopyroxene is inferred to represent unsystematic fluctuations in fluid composition, reinforcing the idea of boundary layer disequilibrium during pyroxene growth (Nakano, 1989).

Grain-size changes are almost always accompanied by a shift in the Fe/Mn ratio (Appendix 2 – MN-25b). This bears a clear relationship with the trace element content, which is a product of the availability of those elements, structural charge balance, and changing partition coefficients with incorporation of Al into the pyroxene structure (Fig. 12; Wood and Blundy, 2001; Bédard, 2014). The resultant micro-scale zonation patterns account for the much of the chemical variance at the outcrop scale.

While trace element contents compositions remain relatively constant within a single pyroxene generation, systematic changes in the REE geochemistry occur during a growth cycle (Fig. 14). Decreases in abundance of ΣREE (+ Y) occur along texturally distinct growth bands and are accompanied by an increase in Eu/Eu*, potentially recording input of fresh fluid to the hydrothermal system (Fig. 14B-C). Variations between pyroxene growth cycles potentially reflect new pulses of REE-rich fluid with negative Eu anomalies, which increase through time. Calcic clinopyroxene should readily incorporate excess Eu^{2+} into its crystal structure, leading to positive Eu anomalies. Since this is not observed, there must be modifications of the availability of Eu^{2+} in the fluid due to: 1) temperature variations, 2) available ligands for transport of Eu^{3+}, 3) depletion of Eu prior to fluid exsolution, or 4) removal of Eu by coeval crystallization of a more favorable mineral phase (e.g., epidote: Sverjensky, 1984; Haas et al., 1995).

The mineral chemistry of pyroxene is directly comparable with existing data from pyroxene skarns in the Madan ore field (Bonev, 2003; Bovay et al., 2015; Vassileva, 2004). Much of the variation in pyroxene composition at a district scale presented in previous works can be contained within clinopyroxene crystals from a single sample, highlighting the need for detailed mineral chemistry to understand prograde distal skarn formation. Other Pb—Zn skarns also exhibit Mn enrichment and compositional variation of pyroxene (Abrecht, 1985; Nakano et al., 1994). Host rock - fluid interactions govern the trace element compositions, resulting in enrichment of Na, Al, and Zn, among other elements, which may indicate proclivity for sulfide deposition within those systems (Nakano, 1998). While whole rock and portable XRF analyses still provide valuable information on element mobility during the lifespan of the system (pre-, syn-, and post- mineralization), they represent an amalgamation of processes including element re-distribution during retrograde overprinting, nugget effects for trace elements such as Be, P, Ti, Zr, and REE + Y, and loss of relative timing information (Appendix 5).

6.4. Growth and chemical evolution of epidote skarns

Epidote skarn distribution is governed by host rock composition and permeability generated by irregular fluid pulses during skarn formation. Because of this, spatial measurements for the epidote skarns (*DC* and *DF*) have little meaning, as epidote growth occurs repeatedly in the same location. The porosity generated in the epidote skarn does not approach the reactive infiltration instability feedback generated in the marble, meaning that limited space is available for voluminous skarn growth. In contrast to the pyroxene skarn, which becomes a (relatively)
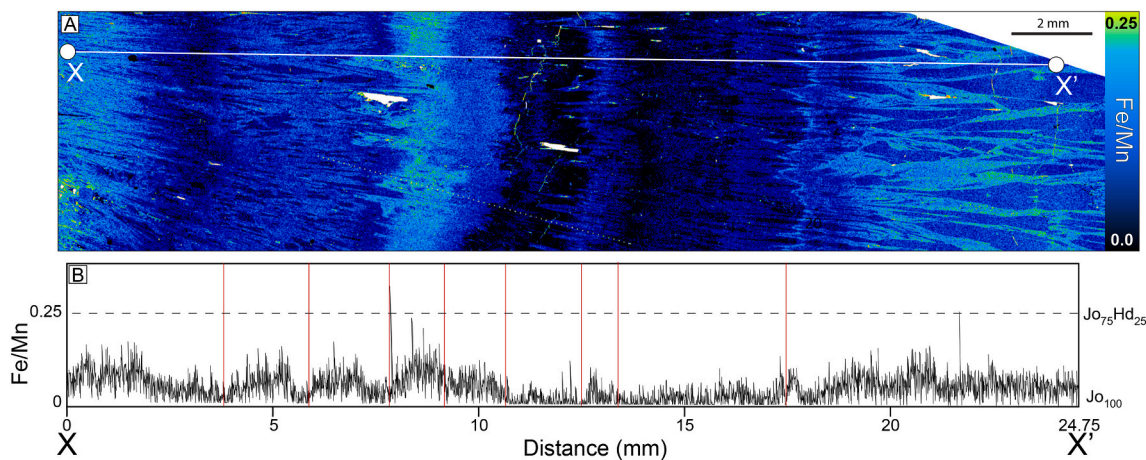

Fig. 13. (A) Fe/Mn ratio map generated using the Image-J software, based on QEMSCAN element intensity maps (MN-108d). (B) Spectrum of Fe/Mn with growth bands outlined along profile X-X'. Red dashed lines correspond to change in Fe/Mn ratio in (A). (For interpretation of the references to colour in this figure legend, the reader is referred to the web version of this article.)
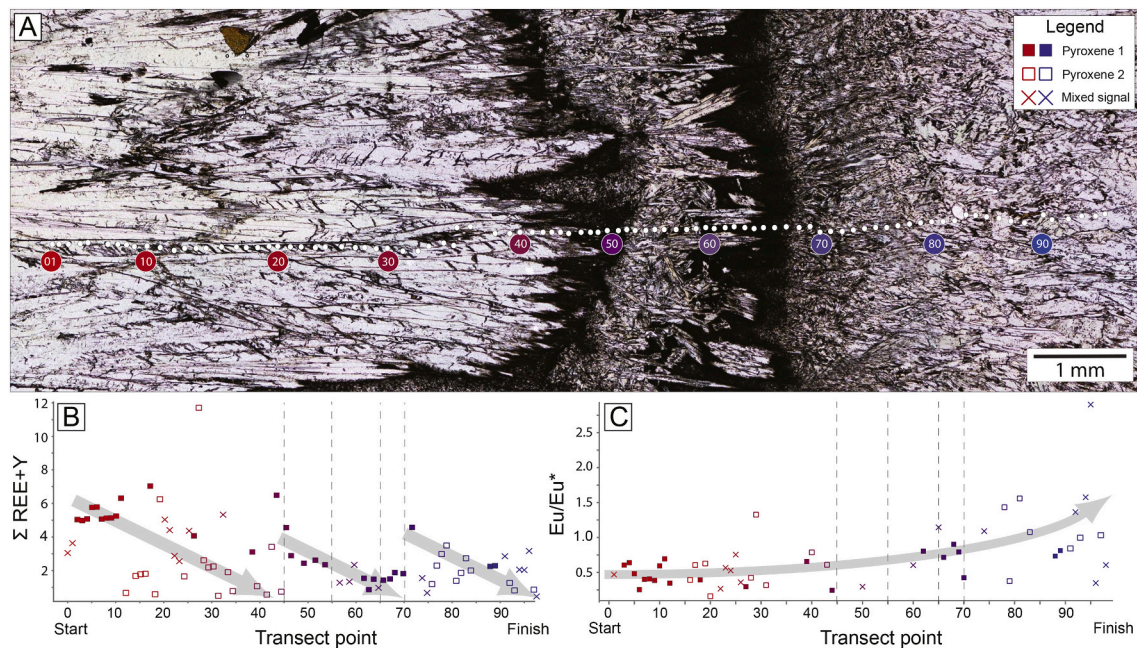
Fig. 14. (A) Transmitted PPL photomicrograph of skarn growth bands and laser ablation profile location (sample MN-25b). (B) Sum of REE (+ Y) plot along laser ablation profile. (C) Eu/Eu* plot along laser ablation profile. Red lines indicate position of texturally defined growth bands. (For interpretation of the references to colour in this figure legend, the reader is referred to the web version of this article.)

impermeable lithologic contact, epidote replacement moderately increases the local porosity with respect to the protolith.

Protolith replacement begins with the destruction of plagioclase and biotite by the metasomatic fluids and the incorporation of their chemical components into a metasomatic assemblage of epidote + K-feldspar (Fig. 5C). A later generation of epidote crystallizes along quartz ± calcite in open space filling, which overlaps with the timing of sulfide mineralization (Fig. 5A, D). During this stage, K-feldspar is replaced by fine-grained white mica (sericite), and both epidote 1 and 2 may be replaced by chlorite.

Epidote generations are best distinguished by the Fe content, which increases by ~0.5 a.p.f.u in the later epidote (Fig. 9A). Calcium for epidote growth was readily available during both stages due to marble dissolution and plagioclase replacement in the host gneiss. The chemical evolution of the system from epidote 1 (Fe ≈ 0.55 a.p.f.u.) to epidote 2 (Fe ≈ 0.95 a.p.f.u.) is reflected in the trace element geochemistry, as Mg and Ti are notably higher in epidote 1, likely retaining the elemental signature of the host mineralogy (biotite) during early stages of replacement. While epidote growth continued, the chemical components in later epidote increasingly reflect fluid input and less of the dwindling remnant Al-silicate phases. Empirical evidence indicates that limited mobility of REE + Y in epidote skarn systems formed in aluminosilicate hosts caps the impact of these elements on the chemical evolution of these skarns when compared to the REE + Y progression of skarn minerals in a carbonate precursor (e.g., Kato, 1999; Xu et al., 2016).

Epidote crystallization spanned the duration of the metasomatic system, an interpretation which is supported by the textural relationships between epidote 1 and 2 and the general similarities between epidote 2 and the retrograde stage of the pyroxene skarn. The positive shift in Mn content from epidote 1 (~5500 ppm) to epidote 2 (~7100 ppm) suggests an increase in Mn availability with ongoing epidote crystallization, also corresponding to an increase in Sr content from an average content of 982 ppm in epidote 1 to 1260 ppm in epidote 2. This can be explained by the release of these elements during the breakdown of clinopyroxene during retrograde metasomatism. Chemical evolution of epidote throughout the skarn formation process (increase in Mn, Sr) may be a product of system cooling and/or telescoping by cooler

hydrothermal fluids (Ahmed et al., 2020). If this is the case, the precedent epidote 1 crystallization overlaps temporally with the prograde formation of the pyroxene skarn.

6.5. Skarn growth model

The distal skarns at Petrovitsa formed via metasomatic reactions by a fluid which arrived via rapid transport along subvertical feeder structures following the schematic evolution outlined in Fig. 15A. Cyclic fluid pulses resulted in hydraulic fracturing and fluid exploitation of lithologic boundaries (arrows, Fig. 15A). Thermochemical interactions between fluid and host rock resulted in selective replacement of reactive mineralogy in both aluminosilicate (Fig. 15B) and carbonate (Fig. 15C) hosts.

Epidote and K-feldspar are the primary replacement products of reactive feldspar and biotite during initial epidote skarn formation. The abundance of these minerals is controlled by the amount of fluid interacting with the aluminosilicate host and the availability of the reactive mineral phases. Prograde epidote metasomatism is associated with an increase in Ca, Fe, and Mn and a decrease of Na content in the host rock, driven by the first generation of epidote (1) + K-feldspar (Fig. 15B, T2). Epidote 1 is generally more Al-rich with higher contents of Mg, Zn, Ti, and V (± REE). Irregular banding in epidote due to Al—Fe exchange suggests multiple epidote growth cycles, in which epidote 1 is eventually overgrown by epidote 2 in the retrograde stage. The less aluminous epidote 2, accompanied by quartz + calcite, clearly overprints the early epidote skarn. The more ferric epidote 2 has higher contents of Na, Mn, Sr, and Pb. The non-cyclic crystallization of epidote is caused by discontinuous fluid flow events, generating epidote growth in different locations at different times based on physical fracturing during hydrothermal events. The sulfide mineralization stage in the epidote skarn occurs in open spaces, and it is accompanied by muscovite (sericite) and chlorite replacement of earlier epidote and feldspar crystals (Fig. 15B, T3).

Dissolution of calcite in the marble horizons (Fig. 15C, T1) resulted in the generation of significant secondary porosity, which in turn promoted fluid flow. This created open spaces along fluid conduits which allowed for the metasomatic growth of johannsenitic pyroxene as
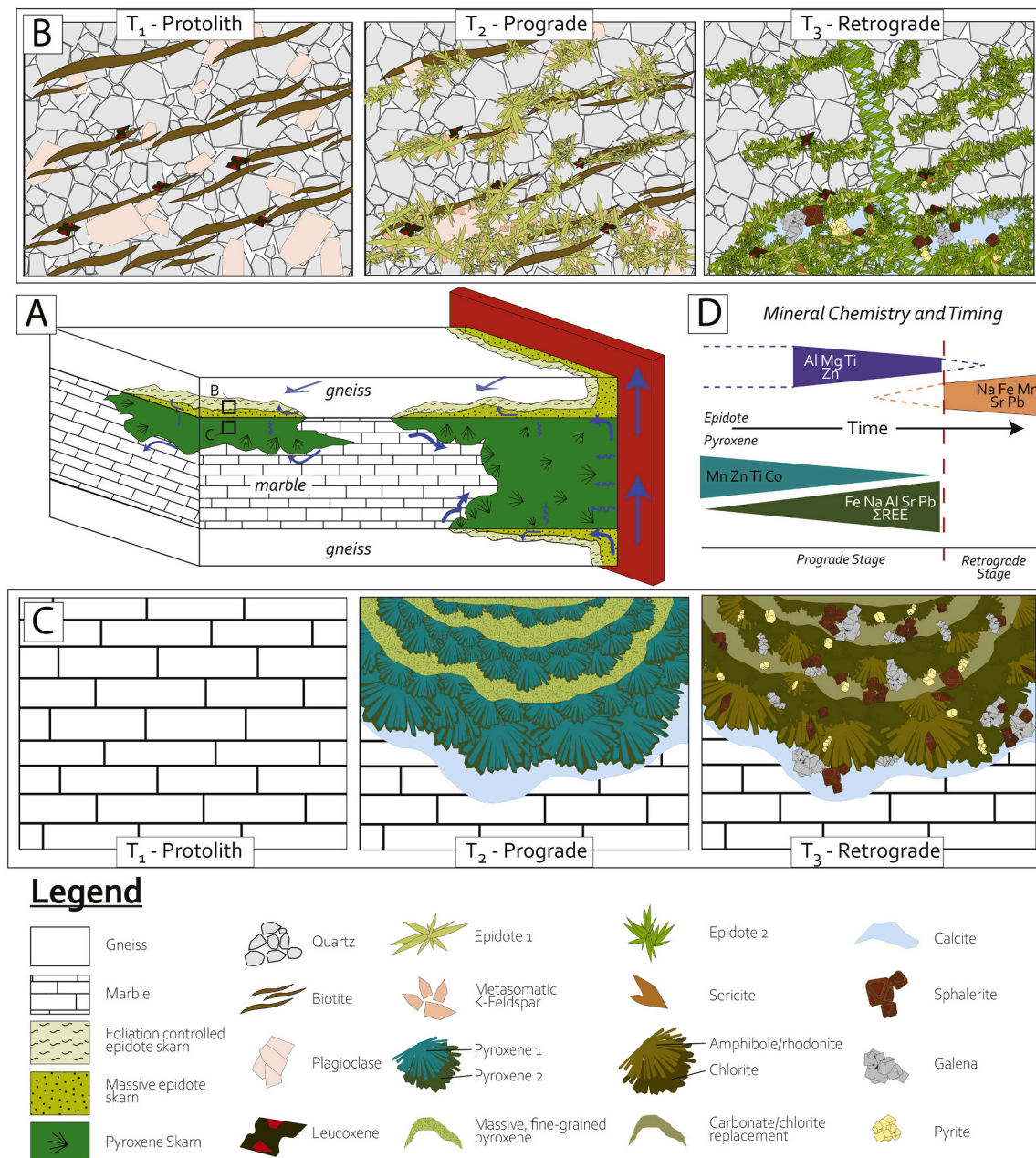
Fig. 15. Distal skarn growth model and depiction of multi-stage skarn growth in both aluminosilicate and carbonate rocks. (A) Block model of the Petrovitsa 865 m North outcrop. Blue arrows indicate fluid flow direction. (B) Time evolution of the aluminosilicate rock during skarnification from protolith (T1) unaltered gneiss to prograde (T2) epidote skarn growth controlled by replacement of plagioclase and biotite to retrograde (T3) epidote skarn formation and sulfide mineralization. (C) Time evolution of the carbonate rock during skarnification from protolith (T1) marble to prograde (T2) pyroxene skarn growth by alternating generations of pyroxene 1 and 2, bounded always at the fluid flow boundary by hydrothermal calcite, followed by the retrograde (T3) and mineralization stage characterized by amphibole + chlorite ± rhodonite and late sulfide replacement (massive or interstitial). (D) General geochemical trends in pyroxene and epidote skarns through time. (For interpretation of the references to colour in this figure legend, the reader is referred to the web version of this article.)

spheroidal aggregates with relatively low permeability (Fig. 15C, T2). Cyclic pulses of skarn-forming fluid resulted in a progressively expanding skarn front, forming growth bands with coherent cyclic features in the pyroxene skarn. During crystallization of a single growth sequence, johannsenite 1 (Jo_{75-85}) crystallized rapidly, incorporating trace concentrations of Zn, Ti, and Co. As fluid chemistry changed and temperature decreased, a more ferrous johannsenite 2 (Jo_{55-65}) crystallized as an overgrowth, incorporating trace amounts of Na, Al, Ga and REE (+ Y). This process was repeated for each successive fluid pulse, corresponding to a skarn formation cycle during the prograde stage. During the retrograde phase, pyroxene was replaced by rhodonite +

bustamite + calcite + quartz ± amphibole, generating interstitial porosity which allowed for more fluid flow in the skarn itself. As the retrograde fluid cooled, sulfide mineralization began, precipitating pyrite, sphalerite, galena and minor chalcopyrite in these cavities, as well as in open space generated at fluid conduits (e.g., the skarn front). Chlorite and bustamite are common alteration products associated with the massive Pb—Zn sulfide mineralization and the selective textural destruction along the growth bands of the pyroxene (Fig. 15C, T3).

The relationship in timing between the formation of the epidote and pyroxene skarns is based on textural evidence linking epidote 2 to the sulfide mineralization. The relative timing of these two events suggests

that early epidote formation was coeval with prograde pyroxene skarn formation (Fig. 15D). Compositionally zoned epidote implies that epidote 2 may even begin at the end of the prograde stage. This relationship links the epidote to the prograde skarn assemblage of the pyroxene skarn, in which both generations of johannsenite are part of the prograde assemblage (Fig. 15D). Chemical trends overlapped and "piggy-backed" on each other, meaning that small scale cyclicity in crystallization led to skarn body-scale chemical evolution. Both epidote and pyroxene skarns formed during prograde metasomatism and acted as favorable hosts for Pb—Zn mineralization.

7. Summary and conclusions

Distal skarn bodies at the Petrovitsa Pb—Zn deposit in Bulgaria record complex growth history and formation driven by cyclic fluid-rock interaction along lithological contacts. Main features, common for pyroxene-dominated distal Zn skarn systems worldwide, can be summarized as follows:

1) Elongate skarn minerals can be quantitatively mapped as versors and used as structural indicators towards more proximal parts of the skarn body with respect to the local fluid conduit. The strongest retrograde overprint and sulfide mineralization are generally found closest to the conduit. The possibility of vectoring towards more proximal mineralization styles remains an attractive application of structural mapping in similar settings.
2) Cyclic growth banding records intermittent fluid pulses and open-system metasomatism (continuous input of new fluids) and is governed internally by closed system process (boundary layer chemical competition) within each cycle. This is expressed by cyclic changes in mineral chemistry at the crystal scale and in growth bands at sample and outcrop scales.
3) Epidote formed during prograde skarn formation generated by metasomatism of aluminosilicate host rocks. This process was less regular and less pronounced than the pyroxene skarn growth due to limited permeability for fluid flow.
4) The degree of fluid-rock interaction is related to the increasing fluid transport distance along lithological contacts. Pyroxene mineral chemistry can be used as a proxy for this using a transport parameter (*TP*), which combines the Fe/Mn ratio (decreasing with increased fluid transport) and Al content (increasing with increased fluid transport) within individual pyroxene crystals.

Declaration of Competing Interest

None

Acknowledgements

Appendix A. Supplementary data

Supplementary data to this article can be found online at https://doi.org/10.1016/j.lithos.2021.106408.

References

Abrecht, J., 1980. Stability relations in the system $CaSiO_3$-$CaMnSi_2O_6$-$CaFeSi_2O_6$. Contrib. Mineral. Petrol. 74 (3), 253–260.

Abrecht, J., 1985. Manganiferous pyroxenes and pyroxenoids from three Pb-Zn-Cu skarn deposits. Contrib. Mineral. Petrol. 89 (4), 379–393.

Ahmed, A., Fisher, L., Pearce, M., Escolme, A., Cooke, D., Howard, D., Belousov, I., 2020. A Microscale analysis of hydrothermal epidote: Implications for the use of Laser Ablation- Inductively couple Plasma - Mass Spectrometry mineral chemistry in complex alteration environments. Econ. Geol. 114 (4), 793–811.

Armbruster, T., Bonazzi, P., Akasaka, M., Bermanec, V., Chopin, C., Gieré, R., Heuss-Assbichler, S., Liebscher, A., Menchetti, S., Pan, Y., Pasero, M., 2006. Recommended nomenclature of epidote-group minerals. *European Journal of Mineralogy*n 18 (5), 551–567.

Arndt, N., Fowler, A., 2004. Textures in komatiites and variolitic basalts. In: Ericksson, P. G., et al. (Eds.), The Precambrian Earth: Tempos and Events. Elsevier, pp. 231–298.

Bédard, J.H., 2014. Parameterizations of calcic clinopyroxene—Melt trace element partition coefficients. Geochem. Geophys. Geosyst. 15, 303–336.

Bonev, I.K., 2003. Marble hosted skarn Pb–Zn ore deposits in the central Rhodopes, Bulgaria. In: Eliopoulos, D.G., et al. (Eds.), Mineral Exploration and Sustainable Development, Proc. 7th Biennial SGA meeting, Athens, Greece, pp. 243–246.

Bonev, I.K., Piperov, N.B., 1977. Ore deposition, boiling and vertical extent of the lead-zinc mineralization in the Madan district. Geologica Balcanica 7 (4), 27–42 (in Russian with English abstract).

Bouquain, S., Arndt, N.T., Faure, F., Libourel, G., 2014. An experimental study of pyroxene crystallization during rapid cooling in a thermal gradient: application to komatiites. Solid Earth 5 (2), 641–650.

Bovay, T., 2016. Distal johannsenite-hedenbergite skarns as an ore-forming environment: Madan. University of Geneva, Bulgaria. *Unpublished MSc. Thesis*. 138 p.

Bovay, T., Kouzmanov, K., Dini, A., Wälle, M., Vassileva, R., Gerdjikov, I., 2015. Distal johannsenite-hedenbergite skarns at Madan, Bulgaria and their link to Pb-Zn mineralization: constraints from trace element analyses in skarn silicates. In: *13th Swiss Geoscience Meeting, Basel*, p. 81.

Burg, J.P., 2011. Rhodope: from Mesozoic convergence to Cenozoic extension. Review of petro-structural data in the geochronological frame. J. Virtual Explor. 42 (1), 1–44.

Burt, D.M., 1974. Metasomatic zoning in Ca-Fe-Si exoskarns. In: Geochemical Transport and Kinetics (AW Hofmann et al., eds.). Carnegie Inst. Washington, Publ, 634, pp. 287–293.

Capitani, G.C., Grobety, H.B., Mellini, M., 2003. Reaction sequences, polysomatic faults and chemical compositions of manganese pyroxenoids from Campiglia Marittima skarn. Eur. J. Mineral. 15, 381–391.

Chang, Z., Meinert, L.D., 2008. Zonation in skarns – complexities and controlling factors. In: *Proceedings of PACRIM Congress 2008,* Gold Coast, Queensland, Australia, 11, pp. 303–306.

Ciobanu, C.L., Cook, N.J., 2004. Skarn textures and a case study: the Ocna de Fier-Dognecea orefield, Banat, Romania. Ore Geol. Rev. 24 (3–4), 315–370.

Cooke, D.R., Wilkinson, J.J., Baker, M., Agnew, P., Phillips, J., Chang, Z., Chen, H., Wilkinson, C.C., Inglis, S., Hollings, Zhang, L., 2020. Using mineral chemistry to aid exploration: A case study from the Resolution porphyry Cu-Mo deposit, Arizona. Econ. Geol. 115 (4), 813–840.

Dabovski, C., Harkovska, A., Kamenov, B., Mavrudchiev, B., Stanisheva-Vassileva, G., Yanev, Y., 1991. A geodynamic model of the Alpine magmatism in Bulgaria. Geologica Balcanica 21, 3–15.

Dipple, G.M., Gerdes, M.L., 1998. Reaction-infiltration feedback and hydrodynamics at the skarn front. Mineralogical Association of Canada Short Course Series 26, 71–97.

Driesner, T., Geiger, S., 2007. Numerical simulation of multiphase fluid flow in hydrothermal systems. Rev. Mineral. Geochem. 65 (1), 187–212.

Einaudi, M.T., Burt, D.M., 1982. Introduction; terminology, classification, and composition of skarn deposits. Econ. Geol. 77 (4), 745–754.

Einaudi, M.T., Meinert, L.D., Newberry, R.J., 1981. Skarn deposits. In: *Economic Geology: 75th Anniversary Volume*, pp. 317–391.

Faure, F., Arndt, N., Libourel, G., 2006. Formation of spinifex texture in komatiites: an experimental study. J. Petrol. 47 (8), 1591–1610.

Guy, B., 1993. Banded Skarns, an Example of Geochemical Dissipative Structure. Unpublished Report. https://hal.archives-ouvertes.fr/hal-00523251/document>.

Haas, J.R., Shock, E.L., Sassani, D.C., 1995. Rare earth elements in hydrothermal systems: estimates of standard partial molal thermodynamic properties of aqueous complexes of the rare earth elements at high pressures and temperatures. Geochim. Cosmochim. Acta 59 (21), 4329–4350.

Hantsche, A., Kouzmanov, K., Dini, A., Vassileva, R., Guillong, M., von Quadt, A., 2017. New U-Pb Age constraints on tertiary magmatism and Pb-Zn skarn formation in the Madan District, Central Rhodopes, Bulgaria. Goldschmidt Abstracts 2017, 1533.

Hantsche, A.L., Kouzmanov, K., Dini, A., Vassileva, R., Laurent, O., 2019. District-scale geochemical signatures of calc-silicate skarn minerals from the Pb-Zn (±Ag, Cu) distal skarn deposits in Madan, Bulgaria. In: *Life with Ore deposits on Earth, Proc. of the 15th Biennial SGA meeting, 2019, Glasgow,* UK, 1-4, pp. 178–181.

Ismail, R., Ciobanu, C., Cook, N.J., Teale, G.S., Giles, D., Mumm, A.S., Wade, B., 2014. Rare earths and other trace elements in minerals from skarn assemblages, Hillside

iron oxide-copper-gold deposit, Yorke Peninsula, South Australia. Lithos 184 (187), 456–477.

Ivanov, Z., Sarov, S., Dimov, D., Klain, L., Mishev, E., Dragiev, Ch., Ilioev, K., Danchev, Z., Vulchev, V., 1987. Main Characteristics and Structure of the Madan Ore Field. -Unpublished Report. Geological Survey, Sofia, p. 25.

Jiang, C., 1993. Etude des alternances récurrentes dans les skarns et des instabilités du front de dissolution/précipation. *Unpublished PhD Thesis*. In: Ecole National Superieure des Mines de Saint Etienne, 195 p.

Kaiser-Rohrmeier, M., Handler, R., von Quadt, A., Heinrich, C., 2004. Hydrothermal Pb–Zn ore formation in the central Rhodopian dome, South Bulgaria: review and new time constraints from Ar–Ar geochronology. Swiss Bulletin of Mineralogy and Petrology 84 (1), 37–58.

Kaiser-Rohrmeier, M., von Quadt, A., Driesner, T., Heinrich, C.A., Handler, R., Ovtcharova, M., Ivanov, Z., Petrov, P., Sarov, S.T., Peytcheva, I., 2013. Post-orogenic extension and hydrothermal ore formation: High-precision geochronology of the central Rhodopian metamorphic core complex (Bulgaria-Greece). Econ. Geol. 108 (4), 691–718.

Kato, Y., 1999. Rare elements as an indicator to origins of skarn deposits: examples of the Kamioka Zn-Pb and Yoshiwara-Sannotake Cu (-Fe) deposits in Japan. Resour. Geol. 49, 183–198.

Kolkovski, B., Manev, D., 1988. Madan ore field. In: Dimitrov, R. (Ed.), The Lead-Zinc Deposits in Bulgaria, pp. 37–64. Sofia, Tehnika. (in Bulgarian with English abstract).

Korzhinskii, D.S., 1968. The theory of metasomatic zoning. Mineral. Deposita 3 (3), 222–231.

Kostova, B., Pettke, T., Driesner, T., Petrov, Heinrich, C.A., 2004. LA ICP-MS study of fluid inclusions in quartz from the Yuzhna Petrovitsa deposit, Madan ore field, Bulgaria. Swiss Bulletin of Mineralogy and Petrology 84 (1), 25–36.

Kotzeva, B.G., Guillong, M., Stefanova, E., Piperov, N.B., 2011. LA-ICP-MS analysis of single fluid inclusions in a quartz crystal (Madan ore district, Bulgaria). J. Geochem. Explor. 108 (3), 163–175.

Kounov, A., Seward, D., Burg, J.P., Stockli, D., Wüthrich, E., 2020. Cenozoic thermal evolution of the Central Rhodope Metamorphic complex (Southern Bulgaria). Int. J. Earth Sci. 109 (5), 1589–1611.

Lentz, D.R., 2005. Mass-balance analysis of mineralized skarn systems: implications for replacement processes, carbonate mobility, and permeability evolution. In: Mineral Deposit Research: Meeting the Global Challenge. Springer, Berlin, Heidelberg, pp. 421–424.

Marchev, P., Moritz, R., 2006. Isotopic composition of Sr and Pb in the Central Rhodopean ore fields: Inferences for the genesis of the base-metal deposits. Geologica Balcanica 35, 3–4.

Marchev, P., Kaiser-Rohrmeier, M., Heinrich, C., Ovtcharova, M., von Quadt, A., Raicheva, R., 2005. Hydrothermal ore deposits related to post-orogenic extensional magmatism and core complex formation: the Rhodope Massif of Bulgaria and Greece. Ore Geol. Rev. 27 (1–4), 53–89.

Megaw, P.K., Ruiz, J., Titley, S.R., 1988. High-temperature, carbonate-hosted Ag-Pb-Zn (Cu) deposits of northern Mexico. Econ. Geol. 83 (8), 1856–1885.

Meinert, L.D., 1987. Skarn zonation and fluid evolution in the Groundhog mine, Central mining district, New Mexico. Econ. Geol. 82, 523–545.

Meinert, L.D., 1992. Skarns and skarn deposits. Geosci. Can. 19, 145–162.

Meinert, L.D., 1997. Application of skarn deposit zonation models to mineral exploration. Explor. Min. Geol. 6, 185–208.

Meinert, L.D., Dipple, G., Nicolescu, S., 2005. World Skarn Deposits. In: Hedenquist, J. W., Thompson, J.F.H., Goldfarb, R.J., Richards, J.P. (Eds.), Economic Geology 100th Anniversary Volume. Society of Economic Geologists, Littleton, Colorado, USA, pp. 299–336.

Milenkov, G., Kouzmanov, K., Hantsche, A.L., Vassileva, R.D., 2019. Retrograde skarn formation and polymetallic mineralization in the Petrovitsa deposit, Madan district, South Bulgaria. Review of the Bulgarian Geological Society 80 (3), 77–79.

Milenkov, G., Vassileva, R.D., Peytcheva, I., Grozdev, V., 2020. U/Pb dating and trace element compositions in pegmatite-hosted titanite from the Petrovitsa Pb-Zn deposit, Madan district, South Bulgaria. Review of the Bulgarian Geological Society 81 (3), 90–92.

Milev, V., Ivanov, Stanev V., 1996. Mining production in Bulgaria 1878–1995. In: Statistical Reference Book. Zemia–93 Press, pp. 1–196 (in Bulgarian).

Nakano, T., 1989. Fluctuation model for compositional heterogeneity in skarn clinopyroxenes. Geochemical Journal 23, 91–99.

Nakano, T., 1998. Pyroxene geochemistry as an indicator for skarn metallogenesis in Japan. Mineralogical Association of Canada Short Course Series 26, 147–168.

Nakano, T., Yoshino, T., Shimazaki, H., Shimizu, M., 1994. Pyroxene composition as an indicator in the classification of skarn deposits. Econ. Geol. 89, 1567–1580.

Ortoleva, P., Merino, E., Moore, C., Chadam, J., 1987a. Geochemical self-organization I; reaction-transport feedbacks and modeling approach. Am. J. Sci. 287 (10), 979–1007.

Ortoleva, P., Chadam, J., Merino, E., Sen, A., 1987b. Geochemical self-organization II: the reactive-infiltration instability. Am. J. Sci. 287 (10), 1008–1040.

Ovtcharova, M., von Quadt, A., Heinrich, C.A., Frank, M., Kaiser-Rohrmeier, M., Peytcheva, I., Cherneva, Z., 2003. Triggering of Hydrothermal Ore Mineralization in the Central Rhodopean Core Complex (Bulgaria): Insight from Isotope and Geochronological Studies on Tertiary Magmatism and Migmatization. In: Mineral exploration and sustainable development -Proceedings of the Seventh Biennial SGA Meeting, Athens, Greece, pp. 367–370.

Ovtcharova, M., von Quadt, A., Cherneva, C., Sarov, S., Heinrich, C., Peytcheva, I., 2004. U-Pb dating of zircon and monazite from granitoids and migmatites in the core and eastern periphery of the Central Rhodopean dome, Bulgaria. In: Abstracts of the 14th annual V.M. Goldschmidt conference: Copenhagen, Denmark, p. A194.

Pacey, A., Wilkinson, J.J., Cooke, D.R., 2020. Chlorite and epidote mineral chemistry in porphyry ore systems: A case study of the Northparkes district, New South Wales, Australia. Econ. Geol. 115 (4), 701–727.

Peytcheva, I., Salnikova, E., Kostitsin, Y., Ovtcharova, M., Sarov, S., 2000. Metagranites from the Madan-Davidkovo dome, Central Rhodopes: U-Pb and Rb-Sr protolite and metamorphism dating. In: *Geodynamics and Ore Deposits Evolution of the Alpine-Carpathian-Dinaride Province. ABCD-GEODE Workshop, Bulgaria*, p. 67.

Rusinov, L., Zhukov, V.V., 2008. Model for the development of rhythmically banded wollastonite-hedenbergite skarns at the Dal'negorsk deposit, southern Russian Far East. Geochem. Int. 46 (8), 789–799.

Sarov, S., Voynova, E., Moskovski, S., Jelezarsky, T., Gerogieva, I., Nikolov, D., Naydenov, K., Nedkova, K., Petrov, N., Markov, N., Marinova, R., Valev, V., 2007. Geological map of Bulgaria 1: 50000, Map sheet K-35-86-G Madan, with explanatory notes. In: *Geology and Geophysics, Ltd.,* Sofia, p. 2007.

Schmid, S.M., Fügenschuh, B., Kounov, A., Maţenco, L., Nievergelt, P., Oberhänsli, R., Pleuger, J., Schefer, S., Schuster, R., Tomljenović, B., Ustaszewski, K., 2020. Tectonic units of the Alpine collision zone between Eastern Alps and western Turkey. Gondwana Res. 78, 308–374.

Shimazaki, H., 1982. The Sasanohastingsite-bearing copper skarn deposit formed in aluminous sediment, at the Yoshioka mine, Japan. Econ. Geol. 77 (4), 868–876.

Sun, S.S., McDonough, W.F., 1989. Chemical and isotopic systematics of oceanic basalts: implications for mantle composition and processes. Geol. Soc. Lond., Spec. Publ. 42 (1), 313–345.

Sverjensky, D.A., 1984. Europium redox equilibria in aqueous solution. Earth Planet. Sci. Lett. 67 (1), 70–78.

Vassileva, R.D., 2004. Compositional variation in the manganoan clinopyroxenes from the Central Rhodopian skarn-Pb-Zn deposits, Bulgaria. In: Proc. 5th International Symposium on Eastern Mediterranean Geology, Thessaloniki, Greece, pp. 1469–1472.

Vassileva, R.D., Bonev, I.K., 2003. Retrograde alterations of manganoan skarns in the Madan Pb–Zn deposits, South Bulgaria. In: Eliopoulos, et al. (Eds.), Mineral Exploration and Sustainable Development. Millpress, Rotterdam, pp. 403–406.

Vassileva, R.D., Atanassova, R., Bonev, I.K., 2009. A review of the morphological varieties of ore bodies in the Madan Pb-Zn deposits, Central Rhodopes, Bulgaria. Geochemistry, Mineralogy and Petrology, Sofia 47, 31–49.

Vezzoni, S., Dini, A., Rocchi, S., 2016. Reverse telescoping in a distal skarn system (Campiglia Marittima, Italy). Ore Geol. Rev. 77, 176–193.

Vidale, R., 1969. Metasomatism in a chemical gradient and the formation of calc-silicate bands. Am. J. Sci. 267 (8), 857–874.

Whitney, D.L., Evans, B.W., 2010. Abbreviations for names of rock-forming minerals. Am. Mineral. 95 (1), 185–187.

Williams-Jones, A.E., Samson, I.M., Ault, K.M., Gagnon, J.E., Fryer, B.J., 2010. The genesis of distal zinc skarns: evidence from the Mochito deposit, Honduras. Econ. Geol. 105 (8), 1411–1440.

Wood, B.J., Blundy, J.D., 2001. The effect of cation charge on crystal–melt partitioning of trace elements. Earth Planet. Sci. Lett. 188 (1–2), 59–71.

Xu, J., Ciobanu, C.L., Cook, N.J., Zheng, Y., Sun, X., Wade, B.P., 2016. Skarn formation and trace elements in garnet and associated minerals from Zhibula copper deposit, Gangdese Belt, southern Tibet. Lithos 262, 213–231.

Yardley, B.W.D., Lloyd, G.E., 1995. Why metasomatic fronts are really metasomatic sides. Geology 23, 53–56.

Yin, S., Ma, C., Robinson, P.T., 2017. Textures and high field strength elements in hydrothermal magnetite from a skarn system: Implications for coupled dissolution-reprecipitation reactions. Am. Mineral. 102 (5), 1045–1056.

Zarayskiy, G.P., Stoyanovskaya, F.M., Balashov, N., 1987. The experimental study of bimetasomatic skarn formation. International Geology Review 29 (6), 629–758.

Zharikov, V., 1970. Skarns (Part I, II and III). International Geology Review 12 (5), 760–775, 541–559, 619–647.